UNIVERSITY OF PADOVA

SCHOOL OF SCIENCE

Department of Geosciences

Director: Prof. Nicola Surian

MASTER'S DEGREE IN

GEOPHYSICS FOR NATURAL RISKS AND RESOURCES

COUPLING OF BOREHOLE AND SURFACE ELECTRICAL RESISTIVITY TOMOGRAPHY – INDUCED POLARIZATION TOMOGRAPHY IN SUPPORT OF HYDRO-GEOLOGICAL SURVEY: THE CASE OF STUDY AT SART – TILMAN, LIEGE, BELGIUM

Supervisor: Prof. Jacopo Boaga

Co-supervisor: Dr. Eloisa Di Sipio

Candidate: Alberto Cogliati

Badge number: 2023378

Session: 2023/24

Index:

1) <u>Abstract</u>.

Negli ultimi decenni, si è largamente diffuso l'utilizzo dei metodi geoelettrici per la caratterizzazione e il monitoraggio dei pozzi trivellati e del loro contesto idrogeologico. È tuttavia importante riconoscere oltre al potenziale dei metodi geoelettrici, ad esempio la naturale sensibilità alla presenza d'acqua, anche alcuni possibili limiti dovuti ai principi fisici dei metodi stessi.

Nell'ambito dello studio di un pozzo trivellato presso Sart - Tilman, Liegi, Belgio, questa tesi si propone di studiare i possibili limiti di sensibilità relativi alla profondità del pozzo e di interpretazione idrogeologica.

La profondità di investigazione necessaria per lo studio del pozzo si contrappone, infatti, alla maggiore sensibilità dei metodi geoelettrici in prossimità degli elettrodi, tipicamente posti in superficie. Per l'analisi di sensibilità, la tesi confronta i risultati ottenuti con e senza elettrodi in pozzo. Oltre alle sezioni di resistività ottenute dall'inversione dei dati, il confronto parte dalla matrice Jacobiana per derivare ed includere anche le sezioni di sensibilità e la covarianza tra le sensibilità dei singoli quadrupoli.

Laddove si abbia sufficiente sensibilità, l'interpretazione deve poi distinguere l'effetto della litologia da quello del variabile contenuto dell'acqua, spesso in mancanza di misure ripetute nel tempo. Per la corretta interpretazione della litologia e l'individuazione della tavola d'acqua, si è considerata la combinazione di resistività e polarizzabilità. I valori relativamente bassi ed omogenei di polarizzabilità ottenuti escludono la presenza di livelli argillosi e indicano che la bassa resistività è quindi attribuibile alla tavola d'acqua, in accordo con i dati idrogeologici a disposizione. L'analisi di sensibilità supporta queste conclusioni ed evidenzia l'importanza degli elettrodi in pozzo.

In recent decades, the use of geoelectrical methods for the characterization and monitoring of boreholes and their hydrogeological context has become widespread. However, it is important to recognize in addition to the potential of geoelectric methods, for example the natural sensitivity to the presence of water, also some possible limitations due to the physical principles of the methods themselves. In the context of the study of a borehole at Sart Tilman, Liège, Belgium, this thesis aims to study the possible limits of sensitivity related to the depth of the well and of hydrogeological interpretation. The depth of investigation necessary for the study of the well contrasts, in fact, with the greater sensitivity of the geoelectric methods in the vicinity of the electrodes, typically placed on the surface. For the sensitivity analysis, the thesis compares the results obtained with and without well electrodes. In addition to the resistivity sections obtained from the inversion of the data, the comparison starts from the Jacobian matrix to derive and include the

sensitivity sections and the covariance between the sensitivities of the single quadrupoles. Where there is sufficient sensitivity, the interpretation must then distinguish the effect of the lithology from the variable water content one, often in the absence of repeated measurements over time. For the correct interpretation of the lithology and the identification of the water table, the combination of resistivity and polarizability has been considered. The relatively low and homogeneous polarizability values obtained exclude the presence of clayey layers and indicate that the low resistivity is therefore attributable to the water table, in agreement with the available hydrogeological data. Sensitivity analysis supports these conclusions and highlights the importance of well electrodes.

2) Geological settings.

2.1) Sart – Tilman geographical and geological framework

My case of study is in a locality called Sart – Tilman. It is a subregion of Liége, Belgium and it hosts the University campus included the department of Applied Sciences. More precisely, Sart – Tilman is in correspondence of the top of a slope in correspondence of the bifurcation of Meuse and Ourthe valleys. The University campus and the site where we performed the surveys are located on the top of the slope of at most 250 m and it is distinguished by a wooded conformation and characterized by a coverage of Oligocene Period sands. Facing the Ourthe valley, there is a flat area corresponding to the Sart – Tilman fluvial terrace, characterised by an alternation of gravel, sand and clayey silt in the upper part while mostly gravelly in the lower part, with an overall thickness of at most 20 m.

An exact delimitation of the Sart – Tilman terrace is difficult to carry out since we tend to confuse its gravelly and sandy lithology with the Oligocene sands of the slope. Hence, the limit between the two is not sharp. Sart – Tilman location, elevation and its fluvial terrace are observed in *Figure 2.1a, 2.1b* (hydrogeological map from Wallonia).
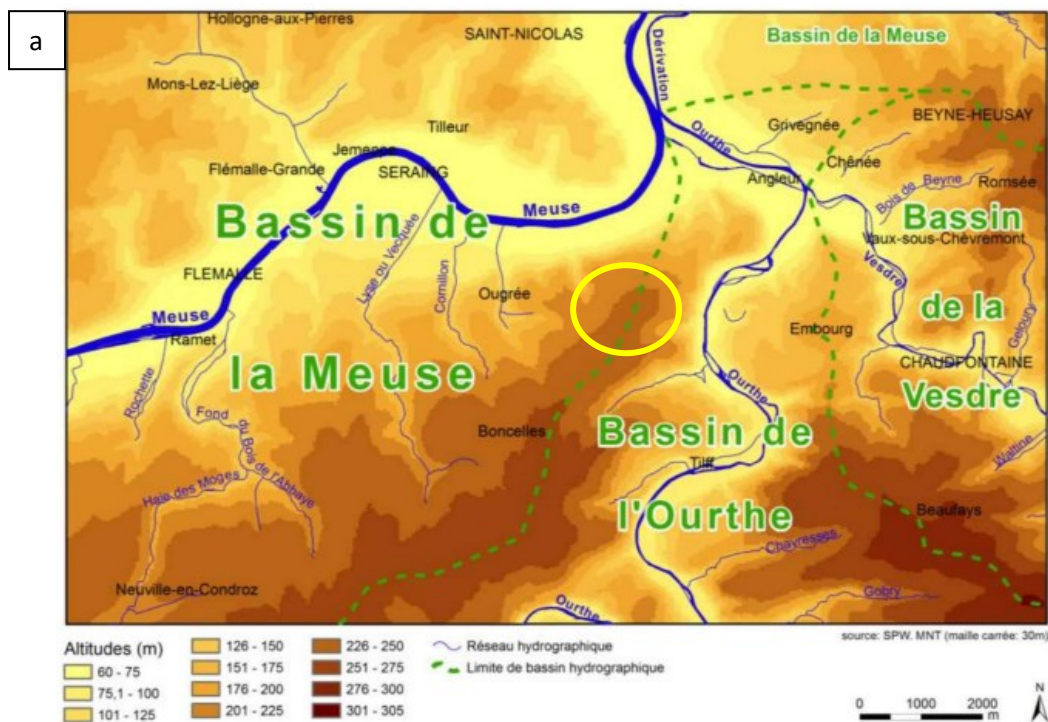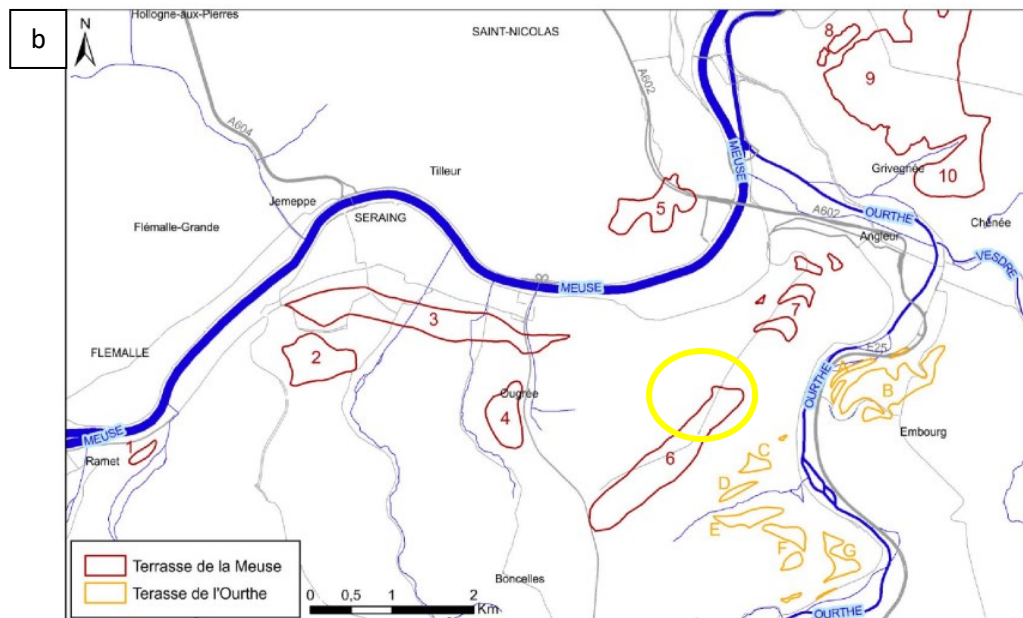
Figure 2.1a and 2.1b - Looking at the first one we can appreciate the position of Sart – Tilman area highlighted by the yellow circle, involving the hillside and the top of the slope reaching a maximum altitude of 250 m. The second picture shows Sart – Tilman position too with the yellow circle but it also shows its fluvial terrace (number 6) facing the South – East side of the hillside.

The first geological map created of the Sart – Tilman area dates to 1897. Then, throughout the decades, it has undergone some modifications by the hand of Prof. Calembert (Calembert et al., 1964; Calembert et al., 1970; Calembert et al., 1974b; Calembert et al., 1975; Pel, 1980). Calembert's deepest contribution to the original version mostly focuses on a further diversification of geological formations of Lower Devonian. These new limits layout between geological formation have been afterwards confirmed either suggested by many drilling sessions.

About the stratigraphy of Sart – Tilman region, from the oldest to the most recent formations, let's start from Lower Devonian Period:

- Upper Siegenian (Pragian), formed mainly of schists, quartzites and micaceous sandstones wine-coloured and variegated, casual green schists and quartzites and, quartzites and light grey micaceous sandstones;
- Lower Emsian (E1), composed of grey or green quartzites and green schists and wine lees plus a few levels of puddingstones. Transition layer between the Lower Emsian and the Middle and Upper Emsian is marked by the persistence of dark sandstone horizons and the clear preponderance of green shales, with intercalations of sandstone and quartzites and wine - coloured shales;

7

- Middle and Upper Emsian (E2-3), they could not be stratigraphically differentiated in the Sart - Tilman domain. Nevertheless, two lithological levels are distinguished:
  I. Lower course (E2-3 inf), formed by sandstone, quartzite, and schist. Layer characterized by its wine colour. It is subdivided into 5 sub-classes according to the proportions of the different types of rocks;
  II. Upper layer (E2-3 sup), composed of large beds of quartzite and green, grey, and brown sandstone. At the top, we have the puddingstone of Burnot. Also subdivided into 5 sub-courses.

Now we can move to the description of the Intermediate Devonian Period of Sart – Tilman stratigraphy:

- Eifelian, formed mainly by red shales. It reaches a thickness of 17 m at Sainval while only a few tens of centimeters at Colonster;
- Givetien, made of puddingstone with calcareous limestone, sandstone with calcareous cement (macigno), coarse sandstone;

To conclude the Devonian Period, we must define the Upper Devonian of Sart – Tilman stratigraphy:

- Frasnian, stage made up of two limestone masses separated by an intercalation of calcareous shale and calcschists;
- Famennian, made of by Famenne shales.

After the Devonian Period there is a discontinuity due to the complex structural features that govern the Sart – Tilman area that brings to the final Series of the Paleogene Period, the Oligocene:

- Oligocene, composed of sands with a gravelly level sometimes split containing quartz and flint pebbles. The bed-rock surface is also sporadically covered with residual Upper Maastrichtian flint.

For the same reason, we face another discontinuity that makes us move directly to the Quaternary Period:

- Quaternary, made up by fluvial deposits (terraces of the Meuse and the Ourthe, see frame geomorphological) and wind silts (loess) and slope silts (colluvium).

The main structural features we can observe in the Sart – Tilman geological map concern the bedrock of the Sart-Tilman region belonging to the northern side of the Dinant Synclinorium. The entire area of the campus is interested by a large syncline having the axis in East – West direction that affects the lower Emsian (Lower

Devonian) layers, with pronounced flooding towards the east. The Lower Devonian geological formations of this zone are characterised by about fifty folds whose three major folds can be recognise (Pel, 1980). Hence, the main structural features of the Sart – Tilman region from North to South are represented by:

- A synclinal fold passing through the northern slope of the Blanc Gravier stream;
- An anticline passing near the Parson stream and the Blanc source of gravel;
- A synclinal fold, particularly well known in the Rocher du Bout du Monde site at Colonster.

Furthermore, from West to East, in the Sart-Tilman – Boncelles area we can still count many others tectonic elements affecting mainly the Upper Emsian geological formations (E2-3 inf and E2-3 sup).

Geological formations we went through that go from Lower Devonian (Pragian) to the Quaternary Periods and the main structural elements of Sart - Tilman area we briefly explained can be seen in the geological map of Sart – Tilman area at *Figure 2.2, 2.3* (hydrogeological map from Wallonia).

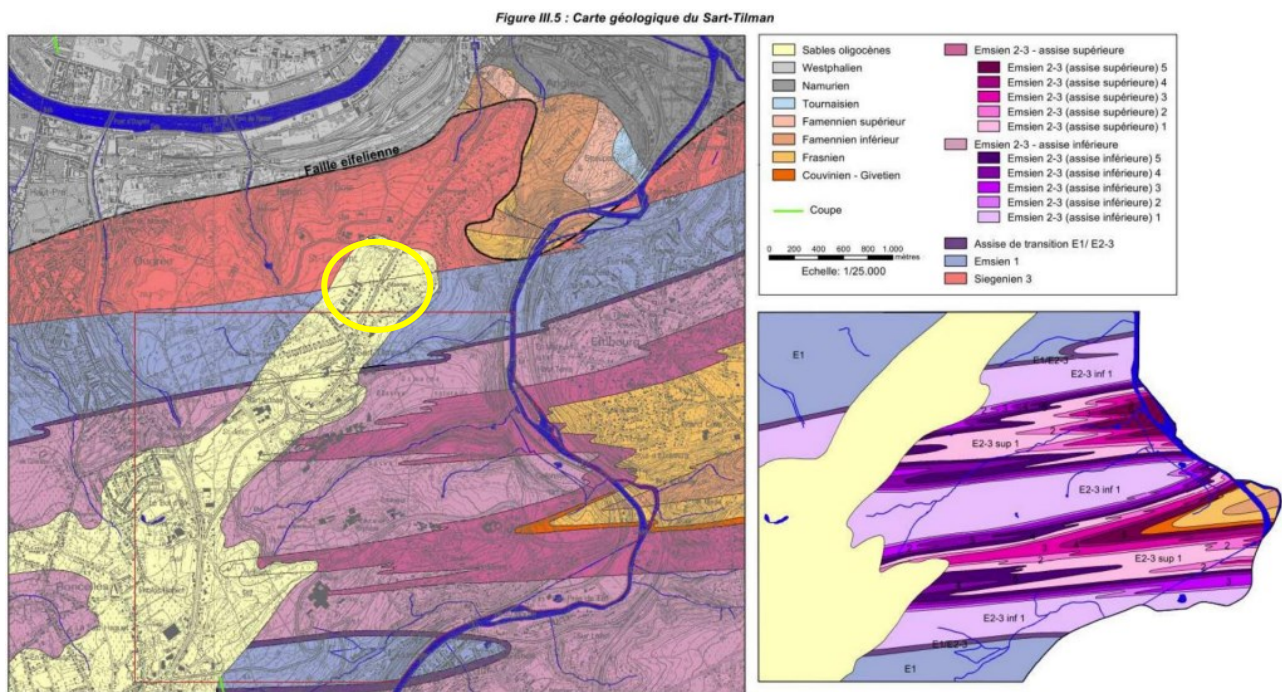Figure 2.2 – This image represents the geological map of Sart – Tilman and the yellow circle highlights the position of the studied site. It shows the various geological formations going from the Lower Devonian (Pragian) to the Oligocene we explain throughout the chapter. We can notice, and it will be confirmed by stratigraphic log and the measures results, that the site is covered by Oligocene sands.
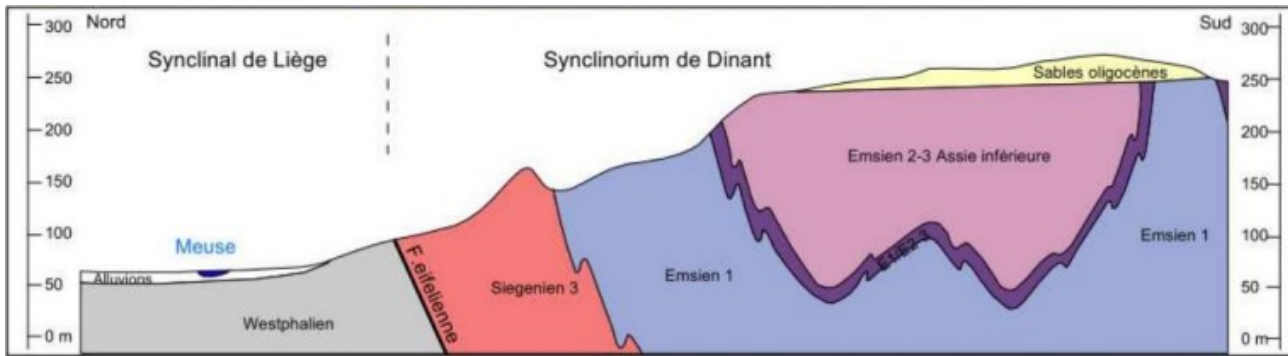
Figure 2.3 – This is the geological section obtain by cutting figure 2.1.2 in North – South direction. In this image we can find the main folding structural features we talked about in the chapter including more the Devonian formations.

2.2) Sart – Tilman hydrological framework.

Sands from the Oligocene Period show a good potential as aquifer, while the above silts from Quaternary Period act as protective layer. It is likely that hydraulic conductivity was modified by the cracks and the consequent weathering within cohesive rocks. Indeed, the fracturing of cohesive rocks may create a further cracks network which encourages the water circulation. The consequence of weathering is a function of the lithology we are considering, and we can distinguish between three main behaviours:

1) For a carbonate, weathering translates in a dissolution of the rock and an enlargement of the existing fracture (and pores) network increasing the average hydraulic conductivity;
2) For a sandstone, weathering returns sand that is characterised by a greater effective porosity which lead to a general increase of the hydraulic conductivity;
3) For a shale or a schist, the alteration produces a clay which tapes the network of fractures reducing drastically the hydraulic conductivity.

Oligocene Period sands concerned in the Sart – Tilman area represent an aquifer with significant potential accordingly to their thickness which is at most of 5 m. Since these sands are located on the top of an elevated plateau, they are feeding the underlying rivers and streams. Throughout the years, porosity and hydraulic conductivity tests were carried out with the purpose of characterise the Oligocene aquifers and it turns out that the total porosity oscillates between 33% and 60% with an average of 47% and that the hydraulic conductivity varies between

$7 \cdot 10^{-5}$ (m/s) and 10^{-7} (m/s) (hydrogeological map from Wallonia).

2.3)   Site scale geological framework.

The investigated site is in the North - East side of the Dinant Synclinorium geological structure. The geological map of Sart-Tilman (Calembert et al., 1964) provides the most recent published geological interpretation of the bedrock and Oligocene sands for the studied area. The well I ran the survey at is located few hundred meters away from the Department of Applied Sciences in the University complex in the Sart – Tilman area, in the correspondence of the Oligocene sands. Since during 2015 there was a drilling campaign, samples lithology was studied. Hence, we now have the chance to exploit the exact stratigraphy of the site, which is:

- From 0 to 2m, dark yellow hard to not hard sand;
- From 2 to 2.4m, very hard layer of flint;
- From 2.4 to 5m, brown sand;
- From 5 to 8m, alternation of light brown to pinkish sandstone and schists;
- From 8 to 16m, alternation of light-dark brown sandstone and schists;
- From 16 to 18m, dark brown sandstones;
- From 18 to 20m, greyish brown sandstone;
- From 20 to 28m, brown to red sandstone;
- From 20 to 32m, fractures in a sandstone bed (recovery of increasingly coarse cuttings).

Furthermore, we can affirm that the first two meters sand belongs to the Tertiary (Oligocene Period), while the thick portion of sand and alternation of sandstone and shales that goes from 5m down to 16m belongs to the Burnotian (Upper Emsian, Lower Devonian) schists - sandstone stage.

Regarding the components of the well, it is composed by a 32 m long PVC tube, about 125 mm of diameter, screened only from 12 m to 24 m deep and from 28 m to 32 m deep. The tube is then surrounded by a square of 1,6 m per side, made of concrete grout until 10,6 m deep, bentonite from 10,6 m to 14 m deep and by a siliceous gravel filter made of grains from 4 mm to 6 mm of diameter from 14 m to 32 m deep. Stratigraphic log and well components can be seen at *Figure 2.4* (Rapport final sur les essais de captage menés au Sart - Tilman).
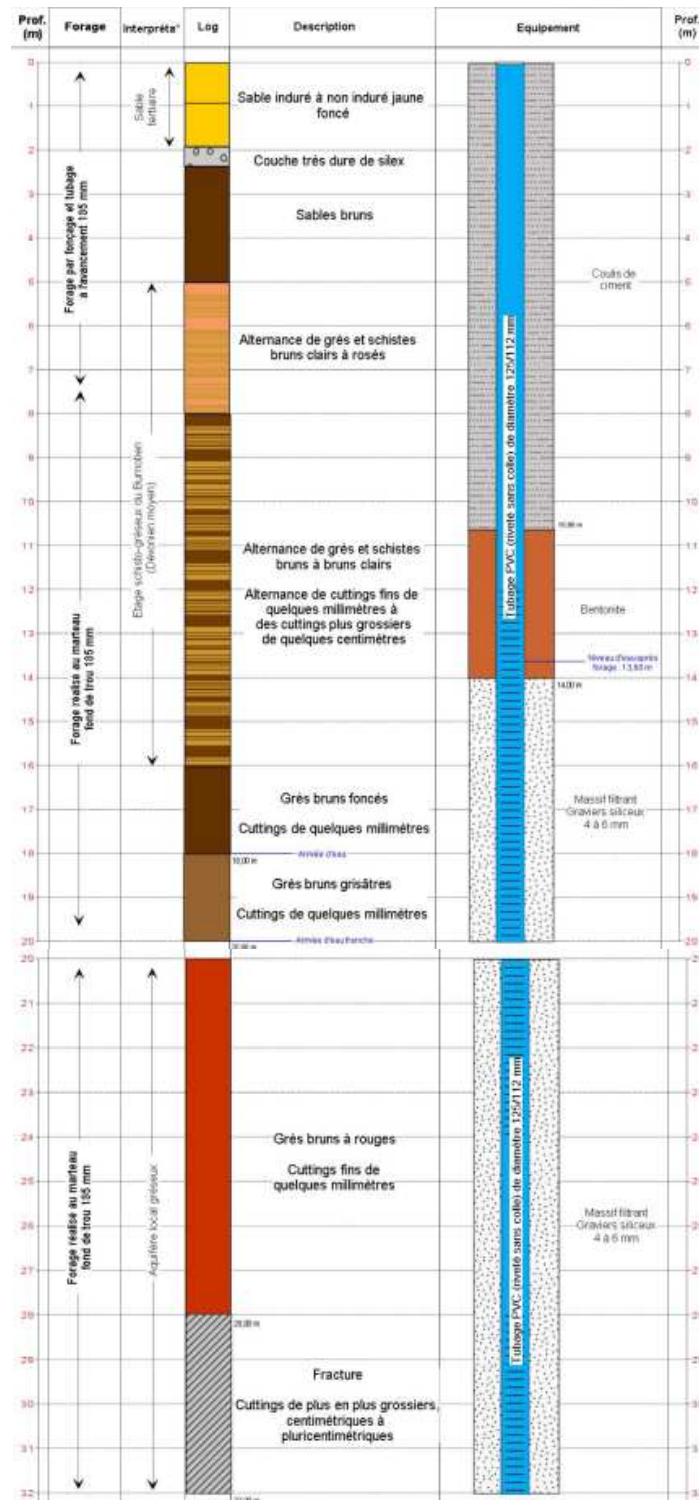
Figure 2.4 – Stratigraphic log resulting from the 2015 drilling session. It shows in detail the sequence between Oligocene sands and Devonian formations, the screening intervals of the borehole and the materials that wrap it.

3) Geophysics: application, theory, and principles.

3.1) A non-invasive investigation tool.

As suggested by the title, Geophysics is a discipline that consists in non-invasive investigations, and it can answer to many issues by as many applications. The main distinction of this discipline is represented by the distinction between active and passive methods. The active ones need the injection of an initial signal into the medium, likely the soil, and the successive sampling of this signal once it has crossed the portion of volume involved in the investigation. We can portrait the earth like a filter which modifies the initial signal as function of its physical, chemical, and biological characteristics. While passive methods just look for some spontaneous signals coming directly from the portion of subsurface, we want to investigate. In this case, we can imagine the earth as a natural source of signal.

Both active and passive Geophysical methods find many pragmatic applications. For instance, we can use non-invasive methods to characterize the lithological sequence of a site, since each layer of the lithology has its own physical characteristics each of them either modify in a different way the initial injected signal, or they emit a distinctive one. We can obtain information about the depth of the water table and about other hydrological parameters as soil porosity and hydraulic conductivity. And, if we match geological and hydrological information, we can obtain a hydro-geological characterization of a specific site. We can understand if a site was contaminated and at what depth the contaminant is since it has got different physical and chemical characteristics than the surrounding soil that make them react differently to the same injected signal. We can use Geophysics to retrieve some fundamental soil parameters for engineering purposes. We can use deep Geophysical investigation methods to identify oil, gas, water, and ores reservoirs, since these four elements have different physical and chemical characteristics than the surrounding geological formations. We can observe saline water infiltration degree in coastal environments for agricultural purposes since electrical conductivity of saline water is higher than fresh water one. Either we can detect and monitor ice presence in permafrost and glacial areas, since ice has got different physical properties than surrounding geological formations, and so on. Furthermore, depending on the budget, on the target and on the purpose of the work, a Geophysical survey can be made in 2D or 3D, on land, in borehole or both at the same time and it can be either punctual or continuous in time as time-lapse and monitoring measurements.

Accordingly, Geophysical investigations strictly depend on and look for the contrast in physical, chemical, and biological characteristics between the target and the surrounding medium. This statement can be resumed by the following fundamental equation:

$$G = G(P, F)$$

Which says that a geophysical quantity (G), measured by the sensors of the instrument (electrode, geophone, antenna etc.) is function of a certain emitted or injected signal (F) and a physical parameter (P). So, depending on the kind of instrument and the physical characteristics of the sampled volume, the instrument initially will gather a distribution of a geophysical quantity (G) as function of a physical parameter (P) and a signal (F). It is important to specify that the initial geophysical quantity distribution (G) is not a convincing representation of the portion of soil we are considering. Infact, the general purpose of the geophysical survey is to work on the acquired raw data to obtain a spatial distribution of the physical parameter, P. To do so, there are two main ways:

1) If we have some a priori information of the site, as the cores from drilling which describe the lithological sequence, that we can use to create a forward model. A forward model is a simulation of the spatial distribution of the physical parameter we are looking for, based on a priori knowledge of the site. It can be explained by the following equation:

$$P = F(M)$$

Where *P* is the distribution of the physical parameter we are looking for, *M* is the input related to the model of the subsoil (a priori information) and *F* is an operator that rules the relation between the model and the distribution of the parameter. So, knowing the site geological features, I can simulate which data I would collect in that investigated portion of subsoil without go on the field and gather any actual measure;

2) If we have not any a priori information of the site, we go through the inverse modelling. The inverse modelling is a procedure concerning an iterative objective function that guides the gradual reduction of the difference between the data of a synthetic model and the measured data, weighted by

the error in the dataset. It ends up with a spatial distribution of the physical quantity we were looking for.

My case of study focuses on a hydrogeological characterization of a site by coupling on land and in borehole measurements of two active Geophysical methods, Electrical Resistivity Tomography (ERT) and Time Domain Induced Polarization (TDIP). In the next paragraphs, I will explain the physical principles that govern the operation of the two geophysical techniques mentioned above, while, in the next chapters, we will talk about how the data was acquired and processed.

3.2) Geoelectric method.

We cannot describe the geoelectric method without mentioning and briefly describing Ohm's law. To start off, Georg Ohm (Erlangen, 16th of March 1789 – Munich, 6th of July 1854) was a German mathematician and a physicist who started to publish his first important works, based mainly on experimental proves, in 1825. On the 1827 he published a fundamental book based on his main empirical observations called "Die galvanische Kette mathematisch bearbeitet" (The galvanic chain worked out mathematically) which explains his theory of the electricity passage within solid materials, among which the theory behind the renowned Ohm's law was revealed.

The empirical homonymous physical law was obtained by applying at the two extremities of a conductor (made of a wire) of known dimension a potential difference with the usage of a battery. It comes out that given a potential difference (ΔV), applied at the two extremities of a conductor, it is directly proportional to the current injected (I) and the resistance of the material itself (R).

$$V = I \cdot R$$

<div align="right">*(Eq. 3.3)*</div>

If we rearrange the initial formula, we can carry the resistance of the conductor out:

<div align="right">*(Eq. 3.4)*</div>

$$R = \frac{I}{\Delta V}$$

Nevertheless, there are two aspects of Ohm's assumptions which are not compatible with the application of the theory for Geophysical purposes. Infact, Ohm considered firstly that the resistance (R) of the material to be constant for the whole dimension of the conductor and so the homogeneity of the medium. Secondly that the resistance depends on the dimension of the conductor itself. If we assume the earth as actual conductor, Ohm's first assumption cannot be relevant since the subsoil has not a constant resistance value due to its heterogenic and anisotropic behaviours, which means that as we move within different soil portions, the measured resistance changes too. Under the second assumption, so considering a cylindrical geometry of the conductor, having total length L and section S, Ohm's law can be expressed in the following way:

$$R = \rho \cdot \frac{L}{S}$$

(Eq. 3.5)

Where R is the resistance of the conductor, expressed in $[\Omega/m]$. It may be important to define the dimension of the body which the current is running through if we are in a laboratory environment. While defining conductors' dimension is not straightforward, on the contrary it is limiting, if we are dealing with geophysical surveys and so with three dimensional heterogeneous and anisotropic conductors as subsoils (often insulating). For this reason, to adapt the Ohm's law for actual contexts, it turns out to be convenient to remove the resistance dependency to the dimension of the conductor. To do so, we consider a conductor of a certain volume having, as before, total length *L*, section area *S* and resistance *R*. We can combine both dimensions length and section area with the original resistance of the body this way:

$$\rho = R \cdot \frac{S}{L} = \frac{1}{\sigma}$$

(Eq. 3.6)

What we carried out is a new parameter called electrical resistivity (ρ), described in Ohm per meter $[\Omega.m]$, which is indipendent from the geometry of the conductor, but it still describes its resistance. The main difference between the resistance (R) and the electrical resistivity (ρ) is that the first one, since it depends on the geometry of the conductor, is not an inherent property of the material, while the second one, since it is conductor geometry independent, is the innate measurable property of a solid material to resist the flow of current through itself, even though

it is not a diagnostic parameter for lithology since resistivity deeply depends on water content and its salinity and rocks physical-chemical characteristics. With the letter σ *(eq. 3.6)* we indicate the electrical conductivity, which results as the inverse of the electrical resistivity ρ and it is described in siemes per meter $[S/m]$. It is an innate measurable property of a solid material as well and it describes the capacity of a material to be passed through by current.

So far, we understood that geoelectric methods in geophysics deal with the injection and the passage of current through a certain volume of soil and the measure of the capability of that soil to resist the flow of current. In the following lines, I will explain the physics that guides the flux of DC current in a conductor.

We described macroscopic form of Ohm's law by differentiating resistance, electrical resistivity, and electrical conductivity. But we can formulate Ohm's law in a microscopic way, by introducing the density current vector, in the general case of an anisotropic conductor, as a soil for instance, which is the most likely scenario we can face:

$$j_x = -\sigma_x \frac{\partial V}{\partial x}$$

$$j_y = -\sigma_y \frac{\partial V}{\partial y}$$

$$j_z = -\sigma_z \frac{\partial V}{\partial z}$$

(Eq. 3.7, 3.8, 3.9)

Where j_x, j_y, j_z are the three dimensions components of the Ohm's vector expressed in scalar way; $\sigma_x, \sigma_y, \sigma_z$ are the electrical conductivity in $[S/m]$ of the medium in the three dimensions, since we are considering an anisotropic conductor; the partial derivatives of voltage (V) with respect to space (voltage gradient) describe the electric field (E), created by the passage of the current itself. To understand how current density changes in space, we just must compute the current density partial derivatives with respect to space, or else the current density divergence since it is a vectorial quantity. What we end up with is a general PDE (called Poisson's equation) that describes the direct current flux at any point in space within a heterogeneous and anisotropic conductor:

$$\frac{\partial}{\partial x}\left(\sigma_x \cdot \frac{\partial V}{\partial x}\right) + \frac{\partial}{\partial y}\left(\sigma_y \cdot \frac{\partial V}{\partial y}\right) + \frac{\partial}{\partial z}\left(\sigma_z \cdot \frac{\partial V}{\partial z}\right) = 0$$

<div align="right">(Eq. 3.10)</div>

Where the partial derivatives with respect to space outside the parenthesis represent the divergence of the current density vector. Then, to simplify the calculus, we may consider the conductor as homogeneous and isotropic, $\sigma_x = \sigma_y = \sigma_z = \sigma$. *Eq. 3.10* turns into:

$$\sigma\left(\frac{\partial^2 V}{\partial x^2} + \frac{\partial^2 V}{\partial y^2} + \frac{\partial^2 V}{\partial z^2}\right) = 0$$

<div align="right">(Eq. 3.11)</div>

We can use this equation to compute analytical solutions for homogeneous systems. Further simplifying for the electrical conductivity, the equation reduces to:

$$\nabla^2 V = 0$$

<div align="right">(Eq. 3.12)</div>

Where $\nabla^2(\cdot)$ is the Laplacian operator, partial second derivatives with respect to space. Since we made unrealistic assumpions on the homogeneity and the anisotropy of the conductor, which led to a simplification of the PDE by omitting the electrical conductivity parameter, the regular nature of the resultant Laplace's equation is not able to fully describe a very specific, realistic heterogenous system. It is just a taste compared to the more complex equations that describe heterogenous and anisotropic systems.

At this point, to inject some current in the soil, which most of the times represents the conductor in geophysics, we need a battery for the current generation and a metal electrode which acts like the punctual source of current. The battery produces an electric current which pass through the electrode and then through a certain soil volume, producing an electric field in the soil that changes in space. If now we consider a simplified scenario concerning a homogeneous and isotropic soil, current flow lines and equipotential lines (lines among which the electric potential (V) has the same value, perpendicular to current lines) spread uniformly in space. Considering two equipotential lines next each other, respectively in position (r) and $(r + dr)$ with respect to the injection point, an infinitesimal

portion of space of spherical shape of dimension dr is carried out and it is interested by a potential described as follows:

$$dV = -\rho \frac{I}{4\pi r^2} dr$$

As described by the latest formula, since the equipotential lines spread within the soil with a spherical geometry, the potential decreases as radius increases, so as we walk away from the electrode. To define the electric potential as function of distance for only one electric source electrode, having a certain position and a random distance (r_i), we simply must integrate the latest equation between r_i and infinite:

$$V(r) = \int_{r_i}^{\infty} \frac{\rho I}{4\pi r^2} dr = \frac{\rho I}{4\pi \, r_i}$$

Where V is the electric potential, ρ is the resistivity of the soil, I is the injected current in the soil and r_i is the distance from the electrode. This formula describes the electric potential as we move out from the punctual source of electric current for a single electrode in an infinite and homogenous space. Nevertheless, if I place the electrode on a homogeneous soil surface, it is more intuitive and likely to assume it as half-space. Thus, the injected current is distributed over half of the portion of space of the original volume, as shown in figure 3.1. This makes double the magnitude of the current density, which makes doubling the electric potential as well:
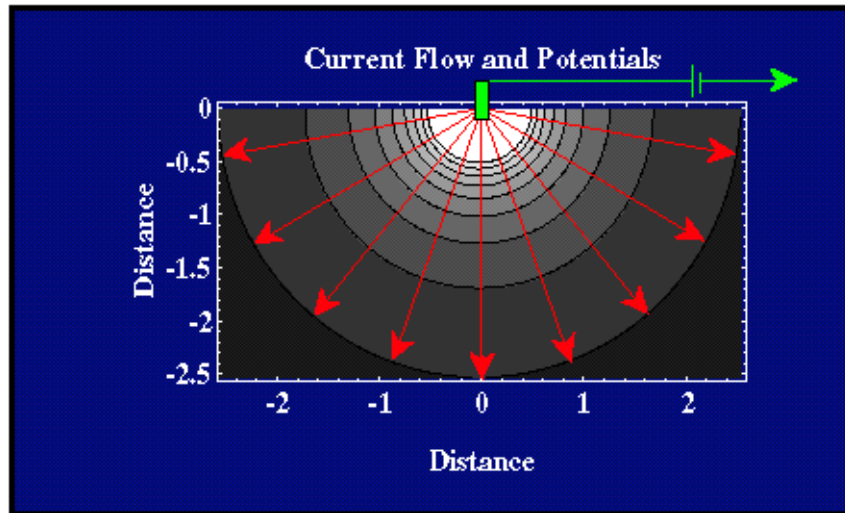
$$V(r) = \frac{\rho I}{2\pi \, r}$$

Figure 3.1 – Current flow lines (red arrows) and equipotential lines (concentric semi-circle) by using a single electrode as source.

We can apply the same concept considering a pair of electrodes as punctual current sources in a homogeneous soil. Infact, due to the linear nature of Laplace's equation, we can simply superimpose the effect of the two electrodes, to compute the resultant electric potential:

$$V_A = \frac{\rho I}{2\pi \, r_A}$$

$$V_B = \frac{\rho I}{2\pi \, r_B}$$

$$V_{AB} = V_A - V_B = \frac{\rho I}{2\pi}\left[\frac{1}{r_A} - \frac{1}{r_B}\right]$$

(Eq. 3.16, 3.17, 3.18)

Where, respectively, A and B are the first and the second electrode; V_A, V_B, V_{AB} are the electric potential measured in corrispondence of electrode A, B and between them; r_A and r_B are the distances from the first and the second electrode.

Nevertheless, what commonly happens on the field while using geoelectric methods is that people work with tools that need configurations made of four electrodes that work in pairs, called quadrupoles. Infact, out of these four electrodes, we must distinguish among two electrodes that act as punctual source of current directly injected into the soil, called current electrodes, and generally indicated with the letters A-B, and the other two electrodes that collect the

potential difference, called potential electrodes and generally indicated with the letters M-N, as we show in figure 3.2.
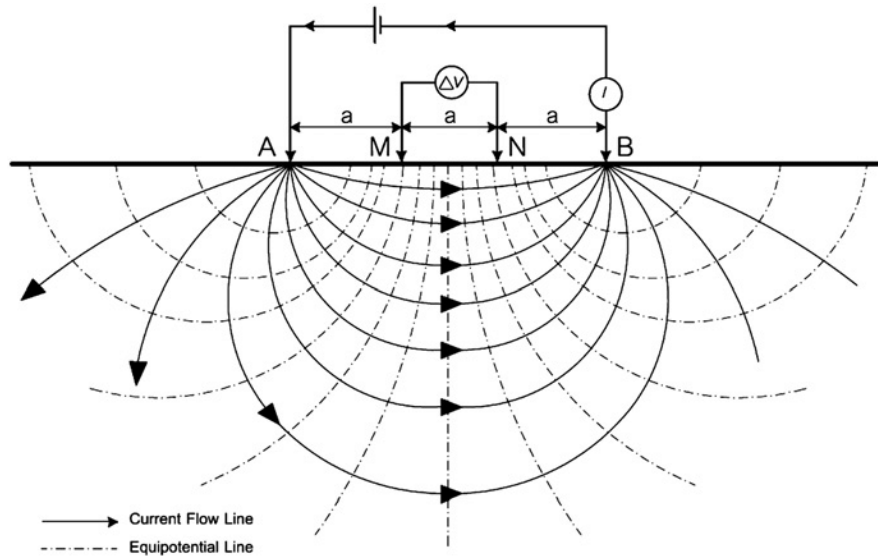

Figure 3.2 – Current flow lines (arrows) and equipotential lines (dashed lines) as product of a quadrupole. Current electrodes A, B inject the current in the subsoil, while potential ones M, N collect the potential difference.

As we did before, we can exploit the linear nature of Laplace's equation to retrieve the electric potential between the two potential electrodes, *M* (or P_1) and *N* (or P_2). To do so, let's define first the electric potential at both potential electrode's locations, considering that injected current has, in A and B respectively, an intensity of $+I, -I$:

$$V_M = V_{MA} + V_{MB} = \frac{I\rho}{2\pi r_1} - \frac{I\rho}{2\pi r_2} = \frac{I\rho}{2\pi}\left[\frac{1}{r_1} - \frac{1}{r_2}\right]$$

$$V_N = V_{NA} + V_{NB} = \frac{I\rho}{2\pi r_3} - \frac{I\rho}{2\pi r_4} = \frac{I\rho}{2\pi}\left[\frac{1}{r_3} - \frac{1}{r_4}\right]$$

(Eq. 3.19, 3.20)

Where r_1, r_2 represent the distances between the first potential electrode (P_1) and the two current electrodes; and r_3, r_4 represent the distances between the second potential electrode (P_2) and the two current electrodes. We can combine the lattest

two equations to get the electric potential sampled between the two potential electrodes:

$$V = V_M - V_N = \frac{I\rho}{2\pi}\left[\left(\frac{1}{r_1} - \frac{1}{r_2}\right) - \left(\frac{1}{r_3} - \frac{1}{r_4}\right)\right]$$

<div align="right">*(Eq. 3.21)*</div>

The reason why the configurations used by the instrument are composed by four electrodes is because the tool is composed by an amperemeter and by a voltmeter and by splitting the quadrupole into two current electrodes and two potential ones, we can create two separate circuits that work independently. More specifically, the first circuit is made by the two current electrodes, the amperemeter and the soil that acts like a resistance and its purpose is to inject the current in the soil. While the second circuit is composed by the two potential electrodes, the voltmeter and the soil and it measures the potential difference between the two potential electrodes. The measure of the potential difference is possible because the voltmeter has got a very high internal impedance, so the potential difference between the two potential electrodes is not affected by the contact resistances. If we considered just two electrodes, which at the same time are current and potential electrodes, we would not be able to sharply distinguish between the previous two circuits. And considering that we don't know the contact resistance between the metal electrodes and the soil, which is generally high (tens of kΩ), the main consequence would be that the contact resistances (one per each electrode) and the soil resistance work in series, making just the soil resistance measure difficult.

Going back to the latest equation *(eq. 3.21)*, we can notice a clear dependency between the measured electric potential between the two potential electrodes and the configuration of the quadrupole. Infact, if we look carefully at the formula, we will see that electric potential is proportional to a geometric factor having the following shape:

$$k = 2\pi\left[\left(\frac{1}{r_1} - \frac{1}{r_2}\right) - \left(\frac{1}{r_3} - \frac{1}{r_4}\right)\right]^{-1}$$

<div align="right">*(Eq. 3.22)*</div>

And since r_1, r_2, r_3, r_4 are distances between potential and current electrodes, this geometrical factor is measured in $[m^{-1}]$. So, the measured electric potential difference is function of the geometry of the quadrupole. Thus, we can define a new parameter called apparent resistivity by rearranging the previous formula:

$$\rho_a = 2\pi \left[\left(\frac{1}{r_1} - \frac{1}{r_2} \right) - \left(\frac{1}{r_3} - \frac{1}{r_4} \right) \right]^{-1} \frac{\Delta V}{I} = k \cdot \frac{\Delta V}{I} = k \cdot R$$

Where K is the geometric factor which depends on the quadrupole configuration, R is the resistance measured by the instrument and the resultant apparent resistivity ρ_a is a linear relation between these two parameters and it represents a correction of the measured resistance as function of the relative position of the electrodes.

To run a geoelectrical survey, the instrumentation can work with many quadrupole geometries. Of course, by changing the geometry of the quadrupole, we change the relative electrodes pairs positioning, the value of the geometrical factor and so the resultant apparent resistivity, but furthermore we can change the depth of penetration, resolution, and sensitivity distribution as well. Let's have a look over the main quadrupole's geometry configurations for the acquisition in geoelectric surveys:

- Dipole-Dipole configuration (figure 3.3) expects to have a separation of current electrodes AB and the potential ones MN, with both pairs located at the extremes of the array. Between AB and MN, the same distance *a* run, while between BM a multiple of each dipole distance runs, called *na*. The estimation of the geometric factor for this configuration is calculated by the following equation:

$$k = 2\pi a n (n + 1)(n + 2)$$

Since dipole-dipole configuration cannot go very deep with the survey, it is not very effective in vertical resolution, while it is in lateral resolution, and it has got a good signal to noise ratio;

Figure 3.3 – Dipole-Dipole configuration.

- Wenner configuration (figure 3.4) expects to have the current electrodes pair AB at the extremes of the array, while the potential electrodes pair is in the middle of the previous two. In this case, each electrode is separated to the next one by a fixed distance equal to *a* and the geometric factor can be calculated by using the following formula:

$$k = 2\pi a$$

Since this configuration enjoys a good degree of penetration, the vertical resolution turns out to be good while the horizontal one is not.
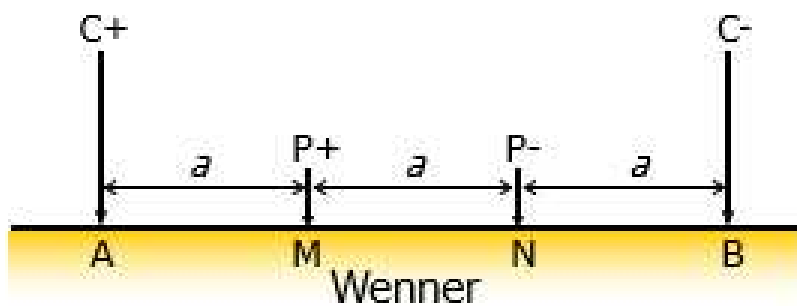

Figure 3.4 – Wenner configuration.

- Schlumberger configuration (figure 3.5) obtains, in terms of lateral-vertical resolution and depth of penetration, intermediate results compared to Wenner and dipole-dipole ones. The current electrodes AB are located at the extremes of the array, while the potential ones are located in between the previous two. Potential electrodes are separated by a distance *a* while current and potential electrodes are divided by a distance equal to *na.* The geometrical factor can be estimated by using the following formula:
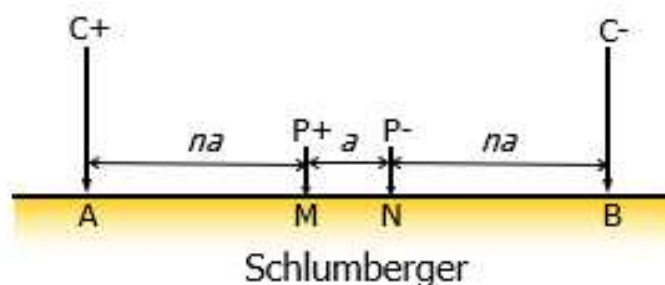
$$k = 2\pi n(n + 1)$$

Figure 3.5 – Schlumberger configuration.

- Multi gradient configuration (figure 3.6) expects to have the current electrodes pair AB at the extremes of the array, while the potential electrodes pair is located between the current ones. Potential electrodes MN are separated by a quantity *a,* while AM distance is equal to a multiple of *na*, a multiple of *a*, and BN distance is equal to *ma*, multiple of *a*. For the estimation of the geometric factor, we need the following formula:

(Eq. 3.27)

$$k = 2\pi \left[\frac{amn(n+1)(m+1)}{m(m+1) + n(n+1)} \right]$$
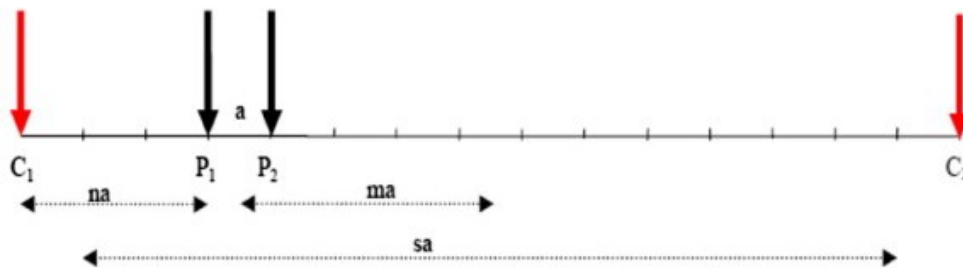

Figure 3.6 – Multi gradient configuration.

In my case of study, we used dipole-dipole and multi gradient configurations.

The kind of current we inject in the subsoil through the current electrodes is a switched square wave. The first reason we use a switched square wave is to avoid any sort of charges polarization on the metal surface of the electrodes, especially the potential ones, otherwise it might create an incorrect shift in the measured voltage. The second reason why we use a switched square wave is to better recognize the Spontaneous Potential (SP), a spontaneous measured voltage produced without any previous current injection, caused by electro-chemical processes occurring between the components of the soil.

An important parameter we must take care of is the distance between the two current electrodes A-B. That is because, as we increase the distance between the two, the injected current goes deeper in the subsoil and vice versa. The current intensity is then ruled by the following equation, for a given current electrode spacing L and a given depth z:

(Eq. 3.28)

$$\frac{I_z}{I} = \frac{2}{\pi} arctan \left[\frac{2z}{L} \right]$$

The actual resistivity of a geological formation is the result of many aspects we must consider if we want to be accurate in the final interpretation. Rocks electrical conductivity assume a wide spectrum of values and it strongly depends on the physical-chemical characteristics of the rock and its saturation condition as explained by Archie's law:

$$\rho_f = \frac{a}{\phi^m S_w^n} \cdot \rho_w$$

Where a (usually near to one) is an empirical constant, m is the cementation exponent (usually near to two), n is the saturation exponent (usually near to two). Overall geological formation electrical resistivity depends on its porosity ϕ that represents the percentage of voids present in the total volume and it is calculated as the ratio between total voids volume and total sample volume. Porosity is important because if we were in dry condition, so the rock is unsaturated, the pores would be filled with air, which has a very low value of electric conductivity $(\sim 10^{-12}\ S/m)$, making the overall electric conductivity of the rock sink. While, on the contrary, if we were in partially saturated or saturated condition, so the rock is either partially or completely saturated by water, the overall electric conductivity would increase because the water is a good conductor. Hence, porosity knowledge is a meaningful aspect for the estimation of the formation resistivity. In the same way, water saturation S_w (water volume over pore volume) and water formation resistivity ρ_w play a fundamental role in the estimation of the overall formation resistivity. Indeed, by increasing the water saturation, average resistivity formation should decrease as well as the formation water conductivity.

3.3)   Electrical Resistivity Tomography (ERT).

Electrical Resistivity Tomography (ERT) is a near surface imaging active geophysical method that expects the injection of current, of switched square wave form, which has the purpose of showing the resistivity distribution in the subsoil after an inversion procedure. This multi electrode automatic acquisition system has been developed starting from the 1990s and it is able to show 2D and 3D resistivity pictures of the subsoil. An ERT survey is the result of an acquisition array made of a certain number of electrodes, depending on the length of the array, the spacing and

the needed investigation depth, which combination forms quadrupoles used for both injection of current and different potential gather. Then resistance is carried out by the application of Ohm's law, so by making the ratio between the injected current value over the measured potential difference. At this stage, apparent resistivity is obtained by the resistance correction for the geometric factor as function of the relative electrodes position, so of the configuration of the quadrupole. Therefore, the instrument makes a continuous, automatic, and sequential data gathering for all the quadrupoles combinations involved in the survey which brings to a single value of apparent resistivity for each quadrupole. A first representation of the apparent resistivity (raw data) distribution can be done by the pseudo section and, even though it is not a true resistivity picture of the subsoil, it can give us an idea of the quality of the data by showing us possible anomalies and main features of the investigated subsoil portion. To get a consistent picture of the subsoil, we must perform an inverse modelling to the raw data.

The gathered data are affected by errors. The kind of errors we can face by using ERT method are mainly two:

- Random error is a casual difference between the observed and true values of apparent resistivity. To fix this kind of error it is enough to inject in the subsoil a switched square wave to avoid any voltage shift in the measures and to stack multiple gathers of the same quadrupole, two in our case, for all the quadrupoles combinations concerned in the acquisition array. Doing so, we end up with a mean value of apparent resistivity affected by a reduced percentage of random error;

- Systematic error is a consistent difference between the observed and true values of apparent resistivity. This kind of error is found in the instrumentation itself and it involves errors in the system gains or calibration of voltage and current monitors, cable leakage and coupling in multiplexers, electrode aging and impedance effects (Douglas La Brecque et al 2007). Given the diversified nature of this error, its processing and resolution are not straight forward as for the random error. A way to deal with systematic error is to exploit the reciprocal measurements. Reciprocal measurements are made by switching current and potential electrodes of the same quadrupole. Theoretically, since the linear nature of the PDE, it ensures us the same measured resistance for both configurations, direct and reciprocal. But these measurements rarely sample the same resistance value, and this difference is due precisely to systematic errors. So, we must compare direct and reciprocal measurements:

$$R_D = \frac{\Delta V_D}{I_D}, \qquad R_R = \frac{\Delta V_R}{I_R}$$

$$R_{AVG} = \frac{R_D + R_R}{2}$$

$$reciprocal\ error = \left| \frac{R_D + R_R}{R_{AVG}} \right|$$

(Eq. 3.30, 3.31, 3.32, 3.33)

We can calculate the reciprocal error for any reciprocal measurement, which normally are the same number of the direct ones, but in my case reciprocals were fewer. At this point, we set a threshold which represents the maximum value that the reciprocal error can assume, so we discard each reciprocal measurement having a reciprocal error bigger than the threshold. By doing so, we should be able to get rid of data deeply affected by systematic error. In my case of study, I worked on random and systematic errors by evaluating the reciprocal error and by applying the Decay Curve Analysis (DCA), both are deeply described in chapter 4.

The two main linked cons of ERT method are the limited maximum investigation depth, which is generally about one fifth of the total length of the acquisition array and it can be reached at the midpoint of the acquisition scheme, and the loss of resolution with depth. For this reason, the choice of the array configuration and its total length must be taken carefully as function of the target and the resolution we want to get at a certain depth since different array configurations bring to different horizontal and vertical resolution and the total length guides the investigation depth.

As in my case of study, we can exploit already existing boreholes to run ERT measurements coupled with on land ones. This double array arrangement guarantees a greater sampled volume of subsoil, a better sensitivity at depth and especially in the vicinity of the borehole, better describing the electrical resistivity distribution along the profile.

3.4) Forward model and Inversion of ERT data.

Before getting into details of both forward and inverse modelling, we must make a premise. Infact, "unfortunately there is no unique solution to this problem, since electrical methods bear a certain degree of inherent non-uniqueness, i.e.,

there typically exists a variety of different models that effectively produce the same response. In addition, because of practical limitations, data are neither complete nor perfectly accurate, but mostly insufficient and inconsistent. Therefore, in principle, an infinite number of models fit the data within a given level of uncertainty. However, by systematically restricting the model search in the inversion process, for instance by claiming predefined model characteristics, a "unique" solution with practical relevance can be obtained. This is usually accomplished by formulating the inverse problem as a regularized optimization problem, which involves minimization of an objective function comprising both data misfit (measured vs. modelled) and a penalty term accounting for deviations from the desired model attributes" (Binley and Kemna, 2005).

Inversion and forward modelling are conceptually different tools although they are guided by the same formulation. Infact, both the forward model and the direct model need, in my case, the application of the finite element method and the subsequent resolution of the Laplace's equation for each element once discretized. The difference in the application is that, for the forward model we refer to a priori geological information of the site, simulating a resistivity distribution that I could measure in that specific acquisition site. While for the inverse modelling we created an initial homogeneous model called direct model which is used in the objective function for the minimization of the differences between the observed resistivity values and direct model ones to get the final resistivity distribution.

Hence, to build a 2D or 3D forward model we must first discretize the domain, so dividing the studied domain in elements (cells) each one having a specific electrical resistivity value and then we must discretize the Laplace's PDE by approximating it numerically obtaining sets of algebraic equations. To do so, we can exploit the concept of difference quotients, which is at the base of the derivatives theory, because it is able to turn a PDE into a system of linear algebraic equations of as many equations as unknowns. Then, by solving the system of linear algebraic equations, we end up with a resistivity distribution described by the changing of resistivity in each element. With different quotients, we can approximate in 3D the partial derivatives of the Laplace's equation in this way:

$$\frac{\partial}{\partial x}\left(\sigma \cdot \frac{\partial V}{\partial x}\right) + \frac{\partial}{\partial y}\left(\sigma \cdot \frac{\partial V}{\partial y}\right) + \frac{\partial}{\partial z}\left(\sigma \cdot \frac{\partial V}{\partial z}\right) = 0$$

(Eq. 3.34)

$$\frac{\partial V}{\partial x} \sim \begin{cases} \dfrac{V_{i+1} - V_i}{\Delta x} \\ \dfrac{V_i - V_{i-1}}{\Delta x} \end{cases}$$

$$\frac{\partial V}{\partial y} \sim \begin{cases} \dfrac{V_{k+1} - V_k}{\Delta y} \\ \dfrac{V_k - V_{k-1}}{\Delta y} \end{cases}$$

$$\frac{\partial V}{\partial z} \sim \begin{cases} \dfrac{V_{j+1} - V_j}{\Delta z} \\ \dfrac{V_j - V_{j-1}}{\Delta z} \end{cases}$$

<div align="right">(Eq. 3.35, 3.36, 3.37)</div>

Eq. 3.35, 3.36, 3.37 are the numerical approximation of the first derivative of voltage with respect to space. The indexes (i, k, j) refer to the positions of three adjacent cells for each dimension which are combined in the linear equation. A step forward to do is including the electrical conductivity in the numerical approximation this way:

$$\left(\sigma \cdot \frac{\partial V}{\partial x}\right) \sim \left(\sigma_{i-\frac{1}{2}} \cdot \frac{V_i - V_{i-1}}{\Delta x}\right), \left(\sigma_{i+\frac{1}{2}} \cdot \frac{V_{i+1} - V_i}{\Delta x}\right)$$

$$\left(\sigma \cdot \frac{\partial V}{\partial y}\right) \sim \left(\sigma_{k-\frac{1}{2}} \cdot \frac{V_k - V_{k-1}}{\Delta y}\right), \left(\sigma_{k+\frac{1}{2}} \cdot \frac{V_{k+1} - V_k}{\Delta y}\right)$$

$$\left(\sigma \cdot \frac{\partial V}{\partial z}\right) \sim \left(\sigma_{j-\frac{1}{2}} \cdot \frac{V_j - V_{j-1}}{\Delta z}\right), \left(\sigma_{j+\frac{1}{2}} \cdot \frac{V_{j+1} - V_j}{\Delta z}\right)$$

<div align="right">(Eq. 3.38, 3.39, 3.40)</div>

Where, the voltage is in correspondence of the node and the current conductivity are located within the elements. Now, if we substitute in *eq. 3.34* the *eq. 3.38, 3.39, 3.40*, what we obtain is:

$$\frac{\partial}{\partial x}\left(\sigma \cdot \frac{\partial V}{\partial x}\right) \sim \frac{1}{\Delta x} \cdot \left(\sigma_{i+\frac{1}{2}} \cdot \frac{V_{i+1} - V_i}{\Delta x} - \sigma_{i-\frac{1}{2}} \cdot \frac{V_i - V_{i-1}}{\Delta x}\right)$$

$$\frac{\partial}{\partial y}\left(\sigma \cdot \frac{\partial V}{\partial y}\right) \sim \frac{1}{\Delta y} \cdot \left(\sigma_{k+\frac{1}{2}} \cdot \frac{V_{k+1} - V_k}{\Delta y} - \sigma_{k-\frac{1}{2}} \cdot \frac{V_k - V_{k-1}}{\Delta y}\right)$$

$$\frac{\partial}{\partial z}\left(\sigma \cdot \frac{\partial V}{\partial z}\right) \sim \frac{1}{\Delta z} \cdot \left(\sigma_{j+\frac{1}{2}} \cdot \frac{V_{j+1} - V_j}{\Delta z} - \sigma_{j-\frac{1}{2}} \cdot \frac{V_j - V_{j-1}}{\Delta z}\right)$$

<div align="right">(Eq. 3.41, 3.42, 3.43)</div>

Every time we do forward modelling, we already know the electrical conductivity (σ) and the spacing between the elements ($\Delta x, \Delta y, \Delta z$). So, voltage values of any element ($V_{i,k,j}$) are the unknowns, combined in linear equations. Hence, this entire equations set (*eq. 3.41, 3.42, 3.43*) aims at just the resolution of voltage in one element ($V_{i,k,j}$). But since any adjacent cell in any direction has got the same equations set, it turns out that any element is composed of similar sets of algebraic equations we have to solve to obtain the voltage in each element. To facilitate the resolution of this linear equation system we assume boundary condition, for instance I can chose arbitrarily to give a null voltage value to the nodes touching the boundary.

Instead, when we solve an inverse problem, we must create first of all a direct model, exploiting the same finite element method and parametrization process used for the forward model. In my case of study, I had to produce a direct model for inverse modelling in 2D and for this reason the initial differential equation we had to work on is not of the same shape of *eq. 3.34*. Assuming that conductivity is constant in the y direction, we apply the Fourier transform in the y direction:

$$v(x, k, z) = \int_0^{\infty} v(x, y, z) \cdot \cos(ky)\, dy$$

<div align="right">(Eq. 3.44)</div>

Where $v(x, k, z)$ is the Fourier transform of the voltage in the y direction. If we plug this equation in *eq. 3.34* this one turns into:

$$\frac{\partial}{\partial x}\left(\sigma \cdot \frac{\partial v}{\partial x}\right) + \frac{\partial}{\partial z}\left(\sigma \cdot \frac{\partial v}{\partial z}\right) - k^2 \sigma v = -\frac{I}{2}\delta(x)\delta(z)$$

<div align="right">(Eq. 3.45)</div>

This is called Poisson's equation, where k is the wavenumber, σ is still the electrical conductivity and $\delta(x)\delta(z)$ repreesent two kronecker's delta. According to kronecker's delta property, only if x, z assumed the values equal to the location of two electrodes, the right part of the equation would be equal to half of the current

intensity, otherwise it turns into zero. At this stage, "finite elements (FE) method was used for the discretization and the analytical solution (of *eq. 3.45*), where the continuous conductivity distribution is approximated by a mesh of individual elements or cells, each with constant conductivity. The potential is then calculated at discrete points (nodes of the mesh) by solving a linear system of equations derived from the discretized differential equation and boundary conditions" (Binley and Kemna, 2005). What we end up with at this stage is a direct model showing a homogenous distribution of electric conductivity, which means that each element of the model contains the same value of electric conductivity equal to $100 \ \Omega.m$, only at the beginning of the inversion. This inverse model involving a flat initial direct model is called Occam inversion.

As we already said, the inverse modelling aims to get a final model showing the electrical conductivity distribution coherent to the raw data we gathered, discretized by a set of homogenous elements (cells) and defined by a model vector m, which is coherent with the observed data and weighted by its errors. This model vector can be represented in the following way:

$$m_i = \sigma_i \ , \ m_i = \ln(\sigma_i) \ , \ (i = 1, \dots, M)$$

Where m_i is the vectorial representation of the electrical conductivity distribution σ_i which may be expressed either in logarithmic or in natural form. Logarithmic form is very common and effective in the representation of the electrical conductivity distribution especially when its range of values is broad. By applying the same concept, we can create a similar vector d made of the observed transefr resistences:

$$d_j = -\ln(R_j) \ , \ (j = 1, \dots, N)$$

Now the inverse problem reduces to find a model m that fits and reproduces the observed data according to its errors. It can be done by an iterative process which involves the use of an objective function of this shape:

$$\psi(m) = \psi_d(m) + \alpha\psi_m(m)$$

As we can see it is the sum of two components. The first one is the expression of:

$$\Psi_d(m) = \sum_{j=0}^{N} \left(\frac{R_j(m) - d_j^*}{\varepsilon_j} \right)^2 = \left\| W_d[f(m) - d_j^*] \right\|^2$$

Where:

- $\Psi_d(m)$ is the iterative objective function and measures the data misfit at each iteration;
- N is the number of measurements we are considering;
- $R_j(m)$ is the number of resistances calculated by the direct model;
- d_j^* is the number of observed resistances;
- ε_j is the error affected by the measured resistances;
- $f(m)$ is the forward operator;
- W_d is the matricial representation of the error in the data (data weighting matrix) which has this form,

$$W_d = diag\left(\frac{1}{\varepsilon_1}, \dots, \frac{1}{\varepsilon_N} \right)$$

Eq. 3.49 is the representation of a least square iterative procedure for the determination of the best set of resistivity value for each cell of the model, to fit the observed data within their error bars, so accordingly to the data uncertainties. So, at the end of each iteration, *eq. 3.49* shows us the data misfit (the residual difference) between the direct model and the measured data. Nevertheless, if we just used the data misfit as objective function, we would end up with two main issues. Firstly, we would have, at the same time, underestimated and overestimated portions of the studied domain that may show unrealistic electric conductivity distribution since this solution is very sensitive to the data uncertainties. Secondly the system itself would be undetermined because it would involve too many unknowns, resistivity elements and too little equations, concerning the measurements. For this reason, we need a further constrain on the inversion to avoid any sort of unlikely electrical conductivity distribution, which includes the introduction of a penalty function in addition to the object function. It is represented by the second term in *eq. 3.48*:

$$\alpha\psi_m(m) = \alpha \left\| W_m(m - m_{ref}) \right\|^2$$

Where:

- α is a scalar quantity that rules both the vertical and horizontal smoothing;
- W_m is the model weighting matrix and it is chosen also to evaluate the roughness $m - m_{ref}$;
- m_{ref} is a reference model that might be the result of a previous inversion in monitoring applications, or just be assigned to a homogenous half space or the null vector if no additional information is available.

Eq. 3.51 can be further splitted as sum of three components:

(Eq. 3.52)

$$\alpha \psi_m(m) = \alpha_s \left\| W_s(m - m_{ref}) \right\|^2 + \alpha_x \left\| W_x(m - m_{ref}) \right\|^2 + \alpha_y \left\| W_y(m - m_{ref}) \right\|^2$$

Penalty for deviation from specified resistivity m_{ref}

Penalty for roughness in *x* and *y* direction

So, W_m (from *eq. 3.51*) incorporates relative contribution of each penalty terms. The whole object function assumes the following shape:

$$\psi(m) = \psi_d(m) + \alpha \psi_m(m) = \left\| W_d \left[f(m) - d_j^* \right] \right\|^2 + \alpha \left\| W_m(m - m_{ref}) \right\|^2$$

(Eq. 3.53)

Adopting an Occam's solution in my case of study, it involves minimizing the whole objective function (*eq. 3.53*) but maintaining the largest value of α possible, thus obtaining the smoothest solution possible. "Minimization of *eq. 3.53* can be achieved through application of gradient search methods. Adopting the Gauss-Newton approach, an iterative scheme results, where at each step, k, the linear system of equations" (Binley and Kemna, 2005):

$$(J_k^T W_d^T W_d J_k + \alpha W_m^T W_m) \Delta m_k = J_k^T W_d^T W_d [d - F(m_k)] - \alpha W_m^T W_m(m_k - m_{ref})$$

(Eq. 3.54)

This linear equation system is solved for the m parameter update at iteration k (Δm_k), the J_k, J_k^T are the sensitivity (or Jacobian) matrix and its transpose, which is equal to:

$$J_{i,j} = \frac{\partial\, d_i}{\partial m_j}$$

It is described as the partial derivative of the measured resistivity as a function of the modelled one. "Starting from a model m_0 (for instance, homogenous or equal to mref, if available), the iteration process $m_{k+1} = m_k + \Delta m_k$ according to *eq. 3.54* is continued for an optimum choice of α (see for example, deGroot-Hedlin and Constable, 1990) until $\psi_d(m_k)$ matches the desired data misfit target value" (Binley and Kemna, 2005).

Thus, the objective function is composed by two main cores, the first one related to the data misfit, and the second one concerning the penalty (regularization) function that guides the smoothing of the model. Since the inverse problem is solved iteratively, at the beginning the data misfit is at its most and a first value of the regularization weight (α) is chosen. At each iteration, both the data misfit and the regularization weight are calculated and the whole process stops when the data misfit converges, so when it assumes a value equal (or very close to) 1, or else when the model obtained is the most compatible with data uncertainties and the smoothest. The meaning of Occam's inversion is to determine the best conductivity set, according to data and its uncertainties, and at the same time to have a smooth distribution of the electrical property.

3.5) Physical phenomena causing Induced Polarization (IP).

The earliest observation of Induced Polarization phenomenon dates to 1913. It was associated to sulphide mineralization, and it was attributed to Conrad Schlumberger. He noticed that if we inject a current within the subsurface containing metallic sulphides and then we interrupt the injection, the potential measured by the potential electrodes M-N does not go down to zero instantaneously, but it takes time to decay. Due to this observation, we understood the basis of mining exploration even though it took a while for the diffusion of the method since the lack of enough performing technology. Nowadays, IP method turns out to be a quantitative tool for the exploration. It is one of the main geophysical methods to discover mineral deposits, especially for porphyry coppers, bedded zinc, sulphides, and gold deposits. Nevertheless, throughout the years its application spectra got wider, including environmental, oil and gas applications. The

main breakthrough was made during the 90s due to the more detailed evolution of technology and instrumentation. It made further diversify the range of application of IP method by including the shallow hydrogeologic characterization of a site and the monitoring of pollutants in a contaminated site.

IP involves a series of transient phenomena when the subsoil is crossed by an electric field created by a quadrupole with the same geometry described for the DC methods. What we may observe during field measurements is that after the energisation of the subsoil the measured potential difference by the two potential electrodes does not go to zero instantly when the current injection is interrupted, on the contrary it takes a certain amount of time to go down to zero. The subsoil thus acts like a capacitor that stores electrical energy by accumulating electric charges on its surface and the time needed for the voltage zeroing is proportional to the polarizability of the subsoil, governed by mineralogic composition and texture of the subsoil, water saturation and its chemical composition.

The electrochemical principles that cause the Induced Polarization phenomenon are mainly two:

1) The electrolytic conductivity expects the movement of ions within a fluid occupying the voids of a geological formation since their pores are totally or partially filled with a fluid, most of the case water, and its solutes as salts. This phenomenon is described by Archie's equation concerning an electrolytic conductivity σ_{el}, the electrical conductivity of the water solution σ_w, the porosity ϕ and water saturation S_w of that specific geological formation,

$$\sigma_{el} = \frac{\phi^m}{a} \cdot \sigma_w S_w^n$$

Where a is a proportionality constant and m, n are related to the cementation and saturation, respectively, for that specific geological formation. It is intuitive that, the higher ions concentration in the fluid, the higher the water and electrolytical conductivity. In this condition, many ion clouds are formed surrounding each ion and when we apply an electrical field to these ion clusters, both central ions and the clouds move but with a time lag, which increases as we increase the frequency of the electric field. The whole ionic polarization process leads σ_{el} to be a real quantity, since the electrolyte cannot be polarized at low frequencies, and σ_w to be complex.

2) The membrane polarization (interface conductivity) expects that the charges can accumulate due to the presence of clay minerals and fibrous or lamellar silicate minerals forming the double layer of charges, each of those negatively charged at correspondence of grains interface or due to the presence of physical restrictions of pores. Under this condition, cations are attracted to the surface of the grains creating a diffuse double layer of charges that consists of the anions of the mineral interface attracting a first fixed cation layer (Stern layer) and a second mobile cation layer of decreasing concentration as we move out the layer. The maximum number of exchangeable cations between the double layer and the electrolyte defines the so-called cation exchange capacity (CEC). The main effects of the presence of the diffuse double layer of charges are firstly a partial obstruction of pores and a further resistance against the current flux and secondly it brings to a polarization phenomenon under the action of an electric field in low frequency domain and it is mathematically described by an imaginary component. The complex interface conductivity (so the imaginary component) is expressed as follows:

$$\sigma_{int} = \frac{h(\sigma_w)S_{\rho or}}{F} \cdot S_w^v(1 + il)$$

<div align="right">(Eq. 3.57)</div>

Where, $h(\sigma_w)$ is a real and usually non-linear function of the salinity of the interstitial fluid, $S_{\rho or}$ accounts for the specific surface area related to the pore volume, F is the formation factor, S_w^v is water saturation whose evponent v is related to electrolytic conductivity σ_{el}, l accounts for the separation of real and imaginary component of the interface conductivity σ_{int}

$$l = \frac{Im(\sigma_{int})}{Re(\sigma_{int})}$$

<div align="right">(Eq. 3.58)</div>

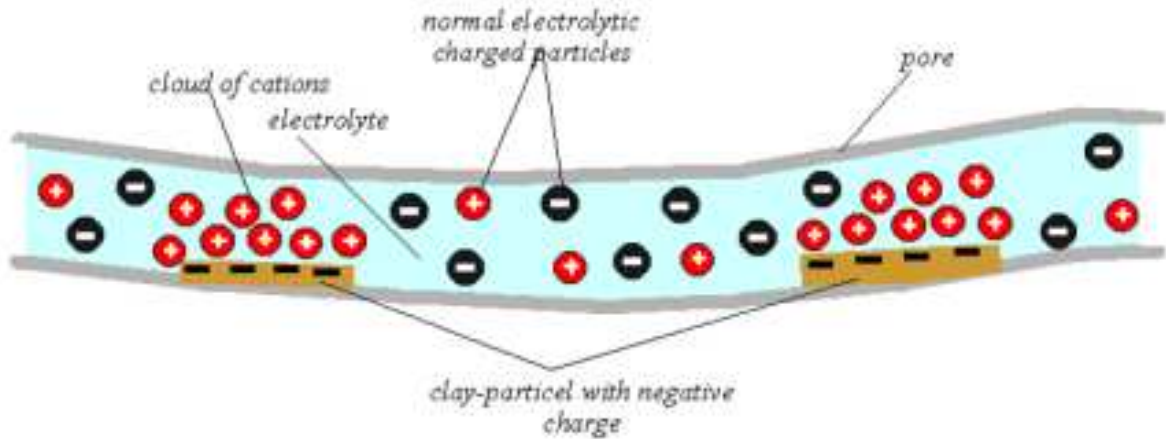Membrane polarization, or interface conductivity, case has a minor effect compared to grain polarization one.

Figure 3.7 – Graphic representation of the membrane polarisation.

3.6) Time and frequency domain Induced Polarization.

Induced Polarization can be measured in both time and frequency domain. Considering IP in time domain, we must observe the shape of the voltage decay curve created when we interrupted the injection of current in switched square wave form (same DC current methods wave). The study of the voltage decay curve, called overvoltage decay times, is at the basis of IP in time domain (TDIP), since we can retrieve chargeability from it, and it is diagnostic of the nature of the subsurface. To calculate the overvoltage effect, we must introduce the apparent chargeability, which is descried as follows:

$$m_a = \frac{V_S}{V_p}$$

Where V_p and V_s are, respectively, the primary voltage and the secondary voltage. But, since the secondary voltage is not easy to define precisely on field, if we want to expand the concept, it turns out that the apparent chargeability can be calculated with the following integral:

$$m_a = \frac{1}{t_2 - t_1} \cdot \frac{1}{V_p} \cdot \int_{t_1}^{t_2} V(t)\, dt$$

Where m_a is the apparent chargeability, expressed in $[mV/V]$, and it estimates how much a medium is chargeable, V_p is still the primary voltage, $V(t)$ is the difference of potential considered within the voltage decay curve and t_1, t_2 represent the time interval over which the integral is calculated for the voltage decay curve and it goes from $0,1s - 10s$.
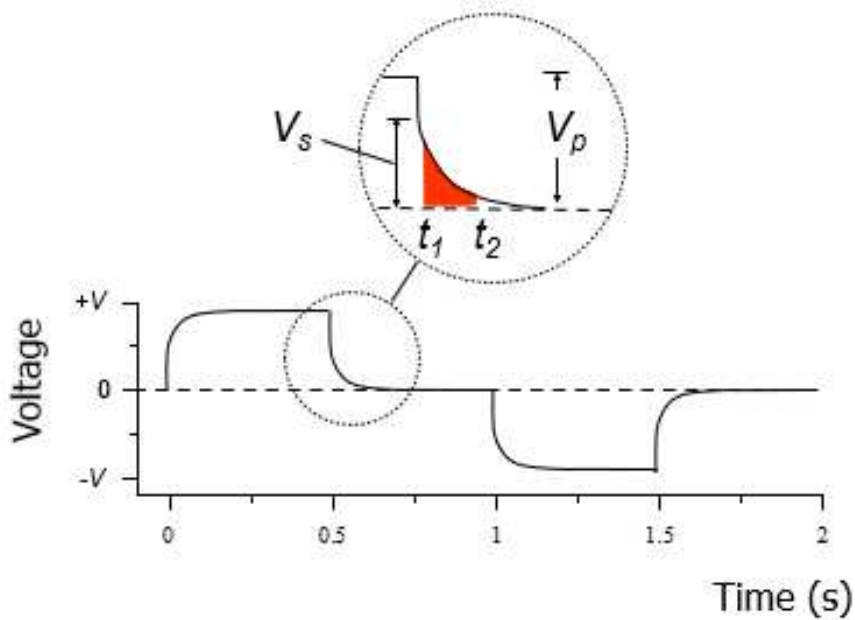

Figure 3.8 – General shape of the switched square wave at a fixed frequency. We can study its voltage decay (overvoltage) to determine the chargeability in time domain.

Induced Polarization can be measured in frequency domain as well (FDIP) by injecting different square wave currents at different frequencies and what is measured are both the amplitude and the voltage. The measured voltage $V(\omega)$ is expressed by the following equation:

$$V(\omega) = R(\omega)Z(\omega)I(\omega)$$

(Eq. 3.61)

Where ω is a certain frequency, $I(\omega)$ is the injected current at that frequency, $R(\omega)$ is a transfer function of the receiving system and $Z(\omega)$ is the ground transfer impedance as function of the quadripole configuration. $Z(\omega)$ infact depends on:

$$Z(\omega) = \frac{\rho_a(\omega)}{G}$$

(Eq. 3.62)

Where, $\rho_a(\omega)$ represents the apparent complex resistivity and G is the actual geometrical factor referring to the quadrupole geometry. Thus, the measured voltage equation turns into:

$$V(\omega) = \frac{R(\omega)\rho_a(\omega)I(\omega)}{G}$$

<div align="right">(Eq. 3.63)</div>

We can refer to *eq. 3.63* in time domain as well, showing that time and frequency domain formulations are linked by Fourier transforms:

$$V(t) = \frac{R(t) * \rho_a(t) * I(t)}{G}$$

<div align="right">(Eq. 3.64)</div>

Where * is the convolution. Since this relation, we might pass from time domain to frequency domain and vice versa.

To run the measurement in frequency domain, a relatively high and low frequencies are used for the investigation. By using the higher frequency, the measured voltage is lower because the overvoltage effect has not enough time to be expressed, while by using the lower frequency we observe the contrary. Due to this effect, we measure different apparent resistivity values as function of the used square current frequency. Thus, the IP effect in frequency domain is frequently described by the Frequency Effect (FE) that theoretically has got the following shape:

$$FE = \frac{\rho_0 - \rho_\infty}{\rho_\infty}$$

<div align="right">(Eq. 3.65)</div>

It is the difference between resistivity magnitudes for frequency values equal to zero and infinite, normalized for the resistivity magnitude value of infinite frequency. Nevertheless, for practical reasons, to calculate FE we must consider the apparent resistivity magnitudes at defined frequencies ω_1, ω_2:

$$FE = \frac{\rho_a(\omega_2) - \rho_a(\omega_1)}{\rho_a(\omega_1)}$$

Where, $\rho_a(\omega_2)$ refers to the apparent resistivity obtained by using the higher frequency and $\rho_a(\omega_1)$ refers to the apparent resistivity obtained by using the lower frequency. Frequency Effect can be expressed as Percent Frequency Effect (PFE) so by multiplying FE by hundred. But, if we consider a small spacing between ω_1, ω_2 such that $\omega_1 \sim \omega_2$, having both frequencies around a certain reference frequency ω_0, the frequency effect can be expressed as follows:

$$FE(\omega_0) = -\frac{\varDelta|\rho|}{\rho_n}$$

In which, $\varDelta|\rho|$ is the change in resistivity magnitude compared to the reference resistivity value $\rho_n = |\rho(\omega_0)|$ obtained at the reference frequency. Another parameter used for the IP effect in frequency domain is the Metal Factor (MF) and we can retreive it by exploiting the parameters of the previous relation:

$$MF = \frac{2\pi \cdot 10^s \cdot FE}{\rho_a(f_2)}$$

3.7) Complex resistivity in frequency domain.

When we previously described the nature of the mechanisms of polarization, it turns out that they can be described by using the complex component of the electrical conductivity (or resistivity). Thus, still remaining in the frequency domain, we can describe the Induced Polarization phenomenon in terms of complex resistivity, also called spectral IP (SIP), by involving the resistivity magnitude $|\rho(\omega)|$ and the phase lag $\varphi(\omega)$, both as function of a certain frequency, which are respectively the representation of the real and imaginary components of the measured apparent resistivity and they may provide many petrophysical parameters of the ground. Also in this case, the IP instrument injects repeated square waves at many different frequencies and then it measures the resulting voltage in time domain. But, to obtain real (resistivity magnitude) and imaginary (phase) components, which are calculated at the fundamental frequency of the square

wave, is not straightforward. First, we can exploit Fourier series to express the voltage $V(t)$ with the Eulerian formulation:

$$V(t) = \sum_{k=-\infty}^{\infty} c_k \cdot e^{ik\omega_0 t}$$

With $V(t)$ measured at time intervals Δt and N_s samples per unit of time. In the same way, we can describe the complex Fourier coefficient c_k:

$$c_k = \frac{1}{N_s} \sum_{i=0}^{N_s-1} V(i\Delta t) \cdot e^{-ik\omega_0 t}$$

$$\omega_0 = \frac{2\pi}{N_s \Delta t}$$

In this case, ω_0 is the fundamental frequency of the square wave. Thus, to describe the voltage in a discrete way, we must find a discrete form of the Fourier transform by rescaling the Fourier coefficient this way:

$$V(k\omega_0) = \Delta t N_s c_k$$

With $k\omega_0$ a discrete frequency. Only at this point, at each discrete frequency, we can get the real and imaginary components of the apparent resistivity $\rho_a(\omega)$ by taking the ratio of the voltage spectrum $V(\omega)$ over the input spectrum $R(\omega)I(\omega)$ (Kemna, 2000). The phase lag can be represented graphically by the time lag between the injected current and the measured votage caused by the polarization phenomena and it can be expressed as follows:

$$\varphi(\omega_0) \sim \frac{\pi}{2} \cdot \frac{d \ln\left(\frac{|\rho|}{\rho_n}\right)}{d \ln\left(\frac{\omega}{\omega_0}\right)}$$

Where, the magnitude of resistivity $|\rho|$ is measured at a certain frequency ω and the reference resistivity ρ_n is measured at the reference frequency ω_0. So, "at any frequency, the resistivity phase is directly proportional to the slope of resistivity magnitude as a function of frequency on double logarithmic scales" (Kemna, 2000).
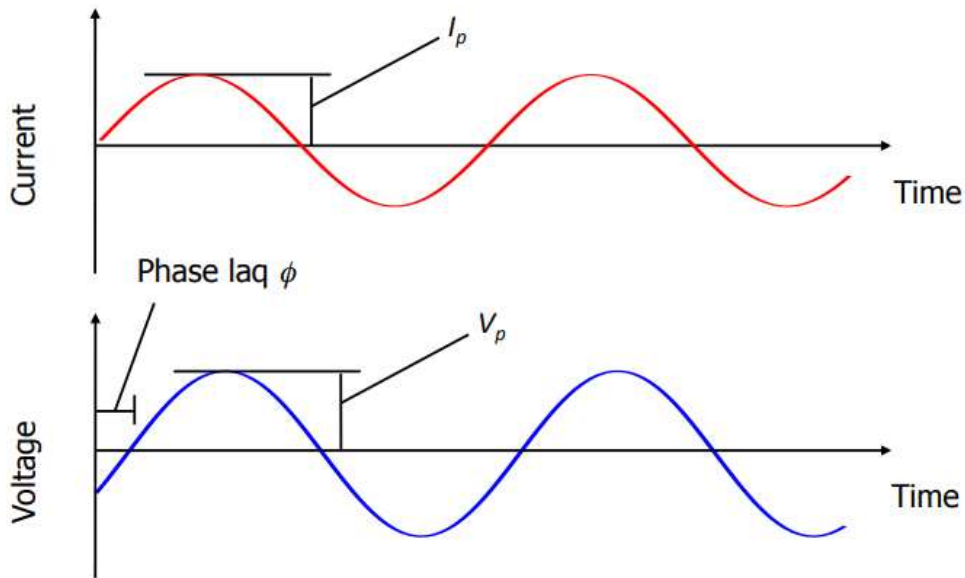

Figure 3.9 – Phase lag as time lag between injected current and measured voltage.

3.8) Complex resistivity in time domain.

Nevertheless, the kind of data we gathered are apparent resistivity and apparent chargeability since we worked in time domain. Indeed, if we acquired IP data in frequency domain, we would have collected the phase angle between induced voltage waveforms and the applied current. Although chargeability and phase angle are collected in different domains, Kemna et al. 1997 described an effective method to convert chargeability in an equivalent phase angle depending on the chargeability sampling and current injection frequency. A typical linear relation that connects the two quantities does exist of the following shape:

$$\phi(mrad) \approx -1{,}3M(mV/V)$$

<div align="right">(Eq. 3.74)</div>

In my case the parameter is equal to -1.673328 according to the executable file kindly Prof. Andreas Kemna provided me with. The coupling of measured resistivity and IP data can be effectively expressed by introducing a complex electrical

conductivity (σ^*) quantity which results in a sum of real and imaginary components of the conductivity:

$$\sigma^* = \sigma' + i\sigma''$$

Where the real conductivity component σ' is the representation of the energy that the system loses with the injection of the current flow in phase with the applied electric field, and the imaginary component σ'' is the quantification of the storage of energy in the system when the displacement current is 90° out of phase with the applied electric field. Hence, the following relations explain how the real and imaginary components of conductivity can relate the measured parameter $|\sigma|$ and the deduced phase lag ϕ from the collected chargeability data:

$$|\sigma| = \sqrt{\sigma'^2 + \sigma''^2}$$

$$\phi = arctan\left(\frac{\sigma''}{\sigma'}\right) \approx \frac{\sigma''}{\sigma'}$$

The approximation for the phase angle relation is valid only if the magnitude of the phase angle itself is little, so considering environments where the polarization effect is small like non-metallic ones, as in our case. It is significant to specify that if we just ran a conventional resistivity survey, the only quantity we would collect is $|\sigma|$, giving us no chance to compute the complex conductivity σ^*. In order to get a direct measure of the surface polarization we have to compute the normalized IP parameters in the following way:

$$\sigma'' = |\sigma| \sin\phi \approx |\sigma|\phi$$

Where the approximation is still valid for low values of phase angle. This relation can be used despite we gathered IP data in time domain since the existing linear relation between chargeability and phase angle described above. Further, we can obtain the real component of conductivity by reversing the measured $|\sigma|$ formula in this way:

$$\sigma' \approx \sqrt{|\sigma|^2 - (|\sigma|\phi)^2}$$

Whereas we are dealing with a non-metallic environment, further confirmed by the resistivity sections, we face two main mechanisms of conduction, electrolytic one (σ_{ele}) which describes the charge transport in the interstitial fluid and surface one (σ_{surf}) that involves a ionic double layer at the interface between grain and fluid. These two kind of conduction are deeply different, such that electrolytic conduction is a pure real term detectable with the usage of a frequency lower than 1kHz and it is guided by the water (or more generally fluid) saturation, the porosity of the formation and the ionic concentration in the interstitial fluid, while surface conduction holds a real and an imaginary component and both depends on the frequency adopted in the survey, the pore size distribution of the material, the chemical composition of the fluid and the mineralogy of the grains. It turns out that the overall complex conductivity can be expressed as a combination of both electrolytic and surface conduction with the following relation:

$$\sigma^* = \sigma_{ele} + \sigma_{surf}^*$$

Where the * exponent describes a complex quantity. We must specify that the real component of the measured complex conductivity is the actual conductivity we collect with a conventional resistivity survey $|\sigma|$ and it is a function of the electrolytic and the real component of the surface conduction. Hence the imaginary component of the complex conductivity depends only on the imaginary component of the surface conduction. It can be resumed by the following relations:

$$\sigma' = \sigma_{ele} + \sigma_{surf}'$$

$$\sigma'' = \sigma_{surf}''$$

By combining these two formulas with the phase angle one, we can calculate the phase response as follows:

$$\phi = arctan\left(\frac{\sigma_{surf}''}{\sigma_{ele} + \sigma_{surf}'}\right) \approx \frac{\sigma_{surf}''}{\sigma_{ele} + \sigma_{surf}'}$$

The approximation is still valid only for small values of phase angle. This relation states that the phase response of a medium is function of electrolytic conduction and both real and imaginary components of surface conduction (Mwakanyamale et al 2012).

3.9)   Forward model and inversion problem.

As we made for the DC current methods, we talk about forward model and the equations we must solve to obtain it. The equations at the basis of the forward model are the same that account for the creation of the direct model in the inversion procedure. In this case, the forward model creates a distribution of complex electric potential since the electric field may be expressed as follows:

$$E = \nabla \phi$$

Where ϕ is a complex potential. Thus, the basis of modelling algorithms is based on the following Poisson equation:

$$\nabla \cdot \big(\sigma(\omega)\nabla\phi(\omega)\big) - \nabla \cdot j_s(\omega) = 0$$

Which is the same equation for DC current expressed in vectorial form, but with the dependence of the phase ω and the presence of a source current term j_s. This Poisson equation, accounts for a 3D case, while we are dealing with a 2D conductivity distribution $\sigma(x, z)$, so we can reduce the Poisson equation in 2D by Fourier transforming the complex potential field along the y direction:

$$\tilde{\phi}(x, k, z) = 2 \int_{0}^{\infty} \phi(x, y, z) \cdot cos(ky)\, dy$$

Where $\tilde{\phi}(x, k, z)$ is the transposed complex potential and k is the real wavenumber. So, Poisson equation reduces to:

$$\frac{\partial}{\partial x}\left(\sigma \frac{\partial \tilde{\phi}}{\partial x}\right) + \frac{\partial}{\partial z}\left(\sigma \frac{\partial \tilde{\phi}}{\partial z}\right) - \sigma k^2 \phi = -I\delta(x - x_s)\delta(z - z_s)$$

Where $\delta(x - x_s)\delta(z - z_s)$ describe two Kronecker's deltas which are related to the electrode position and I describes the injected current. We can solve the previous Poisson equation with adequate boundary conditions. Thus, when $\tilde{\phi}(x, k, z)$ is calculated for a range of wavenumber values, we perform the inverse Fourier transform to get the actual complex potential distribution:

$$\phi(x, y, z) = \frac{1}{\pi} \int_0^\infty \tilde{\phi}(x, k, z) \cdot cos(ky) \, dk$$

Moving to the inverse problem, it is like the case of DC currents. "Any inversion procedure aims to find a model of the subsurface distribution of the relevant physical properties explaining the given observations" (Kemna, 2000). This problem is described by the same formulation of DC current inversion problem, so involving an objective function that we must minimize iteratively:

$$\psi(m) = \psi_d(m) + \lambda\psi_m(m)$$

The main difference with the case of DC currents inverse problem, is that we are dealing with complex quantities, so the inverse solution involves complex calculus. Let's start off by describing the model vector m and the data vector d:

$$m_j = ln(\sigma_j), \quad (j = 1, ..., M)$$
$$d_i = ln(\sigma_{ai}), \quad (i = 1, ..., N)$$

Where σ_j is the complex conductivity of each element of the mesh of the final model and σ_{ai} is the meaured apparent complex conductivity that can be expressed as follows:

$$\sigma_{ai} = \frac{1}{G_i Z_i}$$

Which recalls the Ohm's law and where G_i is the geometric factor according to the geometry of the quadrupole and $Z_i = I_i/V_i$ is the transfer impedance. At this point, we can define the Jacobian matrix as:

$$a_{i,j} = \frac{\partial d_i}{\partial m_j}$$

Similarly, to DC case. Nevertheless, for inverse problems involving real quantities the data noise is one dimensional, while for a complex number, since it is composed by real and imaginary components, the errors affect both dimensions bringing the problem in 2D. Thus, in the objective function the real and imaginary components are given by:

$$\psi_d(m) = \sum_{i=1}^{N} \frac{|d_i - f_i(m)|^2}{(\Delta \ln |Z_i|)^2 + (\Delta \varphi_i)^2}$$

Where:

- d_i denotes the observed data;
- $f_i(m)$ is the operator of the forward solution;
- $(\Delta \ln |Z_i|)^2$ is the real component of the error, it is the natural log of the transfer impedance;
- $(\Delta \varphi_i)^2$ is the imaginary component of the error and it represents the phase.

Throughout the decades, IP methods in time and frequency domain and the Spectral IP found many applications due its dependence with the mineralogical and interstitial fluid composition. Since the beginning of its discovery, IP methods have been used for mineral exploration by looking for polarizable minerals, defining a profitable geological site from ones that are not, and recently this method is giving solid basis for oil investigation. IP methods find a wide application also for hydrogeological and environmental analysis. For instance, in ground water prospecting, the grain size works as guide for the voltage decay curve in time domain and from that it is possible to retrieve the hydraulic conductivity of the

aquifer with the use of many empirical formulas which link the formation factor and the radius of the pores. While, by using SIP, the number of parameters we can assess become even wider, including grain texture, mineralogy, moisture content and electrolyte composition. Under this perspective, clay minerals as montmorillonite and kaolinite, due to their nature and their polarizability capacity, provide a great contribution to IP response. Furthermore, talking about environmental analysis, we can apply SIP in a contaminated site. Infact, contaminants modify the conduction and the polarization properties of the ground, especially the organic contaminants that cannot be mixed up with water since they represent a further separation in phase.

4) Acquisition campaign, Software used and data processing.

4.1) Acquisition campaign.

The purpose of the work is to obtain a hydrogeological characterization of the site exploiting the presence of a borehole. To achieve it, we thought that the best strategy was a coupling borehole-on land of two geophysical methods combination, electrical resistivity tomography and induced polarization in the time domain. It is intuitive to imagine, and we will touch it from a qualitative and quantitative point of view, that the presence of a borehole allows us to reach at depth a good value of sensitivity and so imaging. There is not any other geophysical study related to the site we worked on, so we have not an actual comparison with previous results. The only a priori information we had was a stratigraphic log from the drilling session.

The site we worked on is located at the Liége, Sart-Tilman University campus, a few meters away in South-West direction from the Department of Applied Sciences involving a borehole of 32 m depth. More precisely, the well is located next to a road in a wooded area. In fact, the ground was completely covered by leaves and vegetation which made the coupling difficult with the ground.

Figure 4.1 – Site condition.

Firstly, before going to the site with the whole instrumentation, we had to plan the whole survey by thinking at the adequate array geometry. Thus, we had to decide the total length of the acquisition array, the vertical and horizontal electrode

spacing and the quadrupole configuration, keeping in mind the final target and that we were dealing with a combination of land and borehole ERT and TDIP data acquisition. We came up with an acquisition array geometry concerning a total of 96 electrodes distributed as follows, 64 land electrodes with a spacing of 1,25 m for a total length of 80 m and 32 borehole electrodes, with a spacing of 1m. Land electrodes were classic metal electrodes connected to the cables with metal take outs, while the cable itself worked as borehole electrodes. Even though we placed 32 borehole electrodes, for the whole length of the borehole, we just used 16 of those since the well is screened in two intervals, the first from 12 m to 24 m depth and the second from 28 m to 32 m depth, so that the working borehole electrodes are located just in the correspondence of the borehole screening and consequently the total working electrodes reduce to 80.
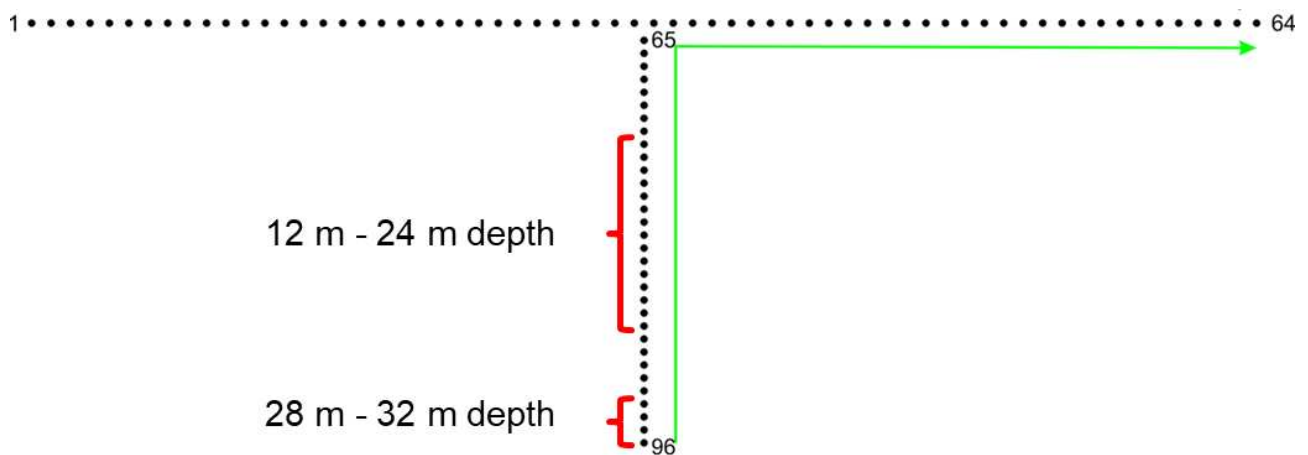

Figure 4.2 – Electrodes disposition: 64 land electrodes and 32 borehole ones for a total of 96. This image also highlights the actual used borehole electrodes by the two red brackets.

After the geometry of the acquisition array, we decided to use dipole-dipole and multi gradient configurations both with increasing skip. Then, we obtained the protocol by using a MATLAB code we wrote, for both the configurations. The instrumentation we decided to use is an ABEM Terrameter LS2 which concerns two main cores, the first one works for the link of the cables of the land electrodes while the second is a switch for the connection of the cables of the borehole electrodes. Overall, to provide the energy necessary to make ABEM Terrameter LS2 work for the total measurements time, we needed an external 12 V battery.

Figure 4.3 – ABEM Terrameter LS2 representation: main core, switch, cables, take outs and connectors.

Only at this point, we were ready to gather the whole instrumentation we needed for the survey and go to the site. Before the placement of the electrodes, we started with a mowing activity for 90m length, since the bushes were so high and thick that I could not place any electrode strongly in the ground. After this operation, with the help of a meter we started to place all the 64 land electrodes, divided into two cables made of 32 electrodes each, and the 32 borehole electrodes, with a lead at the end of the cable to make it be under constant tension. We made sure that the cables were carefully deployed making some loops where it was possible due to the vegetation to avoid any problem of data transmission and simply for an aesthetic reason. Once we connected the cables and the external battery for the energy supply to ABEM Terrameter LS2, we could start the survey.

The first thing we must do is plugging directly into the ABEM Terrameter LS2 the following fundamental parameters and the protocols for the data acquisition:

- The spacing between land and borehole electrodes, respectively of 1,25 m and 1 m;
- Delay time window of 0,8 s and acquiring time (integration time) window of 1,2 s for IP measurements, for a total of 2 s IP time window;
- Consequently, the square current wave was injected at 0,5 Hz for IP method;

- Number of IP windows equal to 20, so each voltage decay curve was divided into 20 bins for their reconstruction;
- A current window from a minimum of 5 mA to a maximum of 200 mA;
- Bad electrodes coupling over 5 $K\Omega$, likely by spilling some salty water on it the galvanic contact should become good enough;
- Failed electrode over 20 $K\Omega$, galvanic contact is insufficient, so we have to remove the electrode and deploy it again;
- Electrode test current equal to 20 mA;
- The stuck number, making the average of the resistivity values. We decided 2 to not spend so much time, the number of involved quadrupoles was pretty high and the IP data takes a lot of time to collect;
- The injection current time for ERT method, a square wave of 250 ms duration, which means a frequency of the injected current about 4 Hz;
- A sample rate equal to 2000 Hz;

Second, we must check if the galvanic contact is good enough, because the general quality of the data depends also on the coupling between electrode and soil. Thus, we let ABEM Terrameter LS2 run a check for the state of the ground resistances, and we noticed that the resistance values were high, in fact we read directly from the screen of the tool that many resistances values were within the window we set previously (5 $K\Omega$ – 20 $K\Omega$), while few of those were exceeding the failure value of 20 $K\Omega$. This means that the coupling between soil and electrode on average is bad, so the capacity of injecting current into the soil is not good enough to gather good quality data. From a practical point of view, the machine was struggling to inject the current in the deeper portion of the soil. Hence, to reduce the value of the ground resistances, we spilled some salty water on each electrode, and, from a further assessment, the resistance values are much lower, so galvanic contact improved.

We ran the resistivity and IP measurements, with their respective reciprocals for a better assessment of the deterministic error in the processing stage. The whole data gathering lasted about 8 hours involving the acquisition of the resistivity data, plus the chargeability measurements for both configurations and respective reciprocals. Intuitively, the IP measurements needed more time than ERT ones, since the instrument must have enough time to determine the chargeability effect in the subsurface by sampling the voltage decay curves within the prearranged time windows of 2 s. We ended up with four text files, the first two files regarding resistivity and chargeability data in dipole-dipole configuration and its reciprocal, same pattern for the last two files but regarding the multi gradient configuration. Direct dipole-dipole file involves 1237 measures while its reciprocal only 175 due to time constraints, while direct multi gradient file concerns 1440 measures and its reciprocal only 215 for the same reason.

4.2) Software used and data processing.

The data processing is divided in two main steps. Firstly, I worked on was a python script that I ran on Spyder, kindly provided by Prof. Nguyen of the Applied Sciences department of Liège University, that refers to the paper of Adrian Flores Orozco et al (2018) about the decay curve analysis. This paper focuses on the study of the voltage decay curves measured in time domain to quantify the error in the IP and transfer resistance data. Error assessment in the data is fundamental to have a good resolution in the final image without any artifact. Indeed, an overestimation of the error in the data would lead to a resolution loss while an underestimation of the data error would produce artifacts in the final image. Errors affecting the data can be recognized as systematic ones, caused mainly by a poor galvanic contact between the electrodes and the ground and by a residual polarization of the potential electrode itself, and random errors, caused by electronic noise of the measuring instrument, etc.

Decay curve analysis (DCA) does not need a further data collection as reciprocals, despite the use of reciprocal measurements is still widespread for the assessment of the error in electrical measures, because collecting as many reciprocals as direct IP measures would double the time for data gathering, from 8 to 16 hours in our case. DCA is especially suitable for multiple gradient configurations, since it enjoys a high S/N ratio, and it does not demand reciprocal measurements. Decay curve analysis is very sensitive to not consider as outliers and delete the voltage decay curves not showing a smooth pattern created by large quadrupoles having low S/N ratio since they are representative of the deepest part of the section. On the contrary, we rather quantify the error in the decay curves and involve it in the final inversion as part of the error model. Furthermore, we might find spatial incoherences between total chargeability values in the dataset that must be deleted before the inversion. Hence, this method relies on the quantification of random error through a decay curve quality check, and on the identification of systematic error through a spatial correlation within the dataset. The whole decay curve analysis is divided into four main steps.

The first one implies a fitting procedure between an exponential model and the actual voltage decay curves, by following this equation:

(Eq. 4.1)

$$m_f(t) = \alpha t^{-\beta} + \varepsilon$$

Where $m_f(t)$ represents the fitted apparent chargeability (mV / V) as function of time after the current shutoff (ms), α and β are the fitting parameters and ε is a

constant we use for any shift from the power law. To understand the quality of the fitting, "we calculate the root-mean-square deviation (rmsd) between the measured and fitted curves" (Orozco et al. 2018) in the following way:

$$rmsd = \sqrt{\frac{1}{N} \cdot \sum_{i=1}^{N} \left(m_f(t_i) - m_{m,i} \right)^2}$$

<div align="right">(Eq. 4.2)</div>

Where N is the number of IP windows of the curve, $m_{m,i}$ is the measured apparent chargeability at times i, $m_f(t_i)$ is the apparent chargeability coming from the power law at time t_i. At this point, we perform the first elimination of those curves in which the voltage increases instead of decreasing in time. While curves related to a large value of rmsd are not deleted yet, since they can be meaningful in the understanding of deep behaviours because they are related to large quadrupoles.

The second step is related to a construction of a reference curve and a second filter to identify any possible spatial incoherence related to chargeability data. To do so, we compute a reference decay curve by taking the median value of the apparent chargeability "of each IP window of the M fitted curves for measurements collected within the same current injection" (Orozco et al. 2018) and it is written as:

$$m_{r,i} = median\left(m_{f,1}(t_i),\ m_{f,2}(t_i),\ ...,\ m_{f,M}(t_i) \right)$$

<div align="right">(Eq. 4.3)</div>

At this point, we can identify and delete the outliers by shifting the obtained reference curve along the vertical axis trying to minimize the rsmd with the actual curve. If the vertical motion of the reference curve is larger than three times the standard deviation of the entire data set, it is an outlier.

The third step involves a standard deviation estimation and the bin analysis. Hence, after the application of the first and second filter, respectively for the estimation of random and systematic errors, we calculate the misfit between the measured decay curve and the modelled one in the first step. The data misfit is defined as:

$$\Delta m_{DCA,i} = m_f(t_i) - m_{m,i}$$

This relation allows us to estimate numerically the erratic behaviour (not smooth decay) of the voltage decay curves. Then, we can model the error in the chargeability data by using the following power law:

$$S_p(m) = aR^b$$

Where the exponent b assumes a negative value since as the transfer resistance increases, the chargeability data error decreases. "We follow the methodology described in Flores Orozco et al. (2012b), based on a partitioning of the data into several bins with respect to the transfer resistance, in which the error model is fitted to the standard deviation computed for each bin. Such procedure honours the assumption that random error can be described by its standard deviation" (Orozco et al. 2018).

The fourth and last step concerns the formulation of the error model for resistance measurements. To obtain it we must fit a rational function with the standard deviation of the apparent total chargeability, divided into beans as in the previous step, described by the formula:

$$s_r(m) = \frac{c}{R} + d$$

Where c, d are simple fitting coefficients, R is the measured transfer resistance and $s_r(m)$ is related to the chargeability error model as function of the transfer resistance. This empirical approach remains faithfull to the assumption that erratic behaviour, caused by random errors, affects voltage decay curves and transfer resistance readings similarly. Hence, we can quantify the error in the transfer resistance data, plugging the same fitting parameters (c, d) but in linear formulation:

$$s(R) = c + dR$$

Where $s(R)$ represents the error model for resistance measurements for the estimation of their error.

By applying DCA script we ended up with four data sets in BERT format ready for the inversion including the total number of both land and borehole electrodes and their location in x and z direction, the number of data points and all the quadrupoles sequence. For each quadrupole, a value of resistance and IP were assigned with their respective errors. For both configurations we kept about the same percentage of data points at the end of the second filtration, 82,23% for multi gradient one and 82,52% for dipole-dipole one. This first result brought us to the conclusion that for both configurations the systematic error is about the same magnitude, which is likely since we did not move any electrode between the two measurements and we spilled salty water before the data gather both times, and that the difference among the two percentages of 0,29% is due to a little variation in random error, which is an acceptable quantity.

However, we realized that DCA is not as suitable for dipole-dipole as for multi gradient configuration. We decided then to determine dipole-dipole data error by using a second method concerning the exploitation of the reciprocal measurements, which I remind you to be much fewer, for dipole-dipole configuration. To do so, we utilized the following python script, kindly provided by Doct. Luca Peruzzo.

```python
import numpy as np

def process_rec(a: np.uint16, b: np.uint16, m: np.uint16, n: np.uint16, x:
np.float64) -> (np.uint16, np.float64, np.float64, np.uint8):
    """
    Reciprocal pairing and check with polarity.
    1 2 3 4
    a m n b d i
    m a b n + j
    m b a n - j
    n a b m - j
    n b a m + j
    """
```

First step of the script is to import the numpy package and to declare a definition called *"process_rec"* which imports five vectors and returns four ones, where unit and float stand respectively for unsigned integer number stored with 16 and 8 bits and for floating-point number format stored with 64 bits. This function aims to estimate the reciprocal error between two data sets checking for quadrupoles pairing and the polarity of the electrodes forming the quadrupoles as briefly explained in the above red lines.

```python
    len_sequence = int(len(x))
    rec_num = np.zeros_like(x, dtype=np.uint16)
```

```
    rec_avg = np.zeros_like(x, dtype=np.float64)
    rec_err = np.zeros_like(x, dtype=np.float64)
    rec_fnd = np.zeros_like(x, dtype=np.uint8)
    for i in range(len_sequence):
        if rec_num[i] != 0:
            continue
        for j in range(i + 1, len_sequence):
            polarity = 1
```

"rec_num" is an initial vector formed by zeroes of the same length vector x where the position of the reciprocal measure will be saved; *"rec_avg"* is the vector that will acquire the value of the average between the direct and reciprocal measures; *"rec_err"* is the vector to which it will be assigned the reciprocal error between the two measures; *"rec_fnd"* is a flag that shows if a measure has already found its reciprocal and if the measure itself is a direct or a reciprocal one. To distinguish between the three cases, rec_fnd can assume the value of 0, 1, 2 which respectively means that there is not any reciprocal for that measure, the measure is direct, and the measure is reciprocal. For each measure, so from index i equal to one to the length of the sequence, we must check if rec_num vector has got a non-zero value. Indeed, if the i-th value of rec_num is non-zero, that measure has already found its reciprocal. Whereas, if rec_num has a value equal to zero at a certain i-th iteration, considering another index j starting from i+1, we find rec_num reciprocal starting from the i-th position on.

```
            if a[i] == m[j] and b[i] == n[j] and m[i] == a[j] and n[i] == b[j]:
                polarity = 1
            elif a[i] == m[j] and b[i] == n[j] and m[i] == b[j] and n[i] ==
a[j]:
                polarity = -1
            elif a[i] == n[j] and b[i] == m[j] and m[i] == a[j] and n[i] ==
b[j]:
                polarity = -1
            elif a[i] == n[j] and b[i] == m[j] and m[i] == b[j] and n[i] ==
a[j]:
                polarity = 1
            else:
                continue
```

These are the possible electrodes combinations for the identification of the reciprocal measures with the respective polarity. Continue means go to the next iteration.

```
            if rec_fnd[j] == 2:
                print("a second direct measurement would match this reciprocal:
", j + 1)
                print("ignore and look for a yet-to-match reciprocal")
                continue
```

58

The if loop checks and warns us if the j-th value of the vector rec_fnd has value two, so if that measure was already used as reciprocal one for two direct measures. If so happens, we keep iterating to look for a fourth not paired yet measure.

```
avg = (x[i] + (polarity * x[j])) / 2
err = abs(x[i] - (polarity * x[j])) / abs(avg) * 100
```

Now we start with the calculation. First, we compute the average between the direct resistance at i-th position *"x[i]"* and the reciprocal one at j-th position *"x[j]"* corrected for the correct polarity. Then we compute the actual percentual reciprocal error through the ratio between the absolute value of *"x[i]"* minus *"x[j]"* corrected for the polarity over the absolute value of the just calculated average.

```
if polarity == -1:
    print("fixing polarity")
    print(a[i], b[i], m[i], n[i], x[i], avg, err)
    print(a[j], b[j], m[j], n[j], x[j], avg * polarity, err)
```

This if loop works as a check, advising us if the reciprocal (index j) of a certain quadrupole (index i) has inverse polarity.

```
rec_num[i] = j + 1
rec_num[j] = i + 1
rec_avg[i] = avg
rec_avg[j] = avg * polarity
rec_err[i] = err
rec_err[j] = err
rec_fnd[i] = 1  # mark meas as direct
rec_fnd[j] = 2  # mark meas as reciprocal (keep 0 for unpaired)
break
```

Now we have to fill the vectors we created initially filled of zeroes. The first two *"rec_num[i]"* and *"rec_num[j]"* save the position of the direct and reciprocal measures (we wrote i+1 and j+1 because the vectors start from position zero); The next two vectors *"rec_avg[i]"* and *"rec_avg[j]"* save the average value in the correspondence of the direct (i index) and of the reciprocal measures (j index). The latest is again multiplied by polarity because we don't want to save it assuming the direct measure polarity, but its original one as reciprocal; The error is percentual so it is the equal for vector in both positions *"rec_err[i]"* and *"rec_err[j]"*; Lastly, *"rec_fnd[i]"* and *"rec_fnd[j]"* stores the position of direct and reciprocal measure, respectively. Rec_fnd[j] assumes a zero value if during the loop no reciprocal measure was found.

```
Cnts = np.bincount(rec_fnd)
if len(Cnts) == 1:
    unpairedCnt = Cnts[0]
    assert unpairedCnt == len(rec_fnd)
elif len(Cnts) == 3:
    unpairedCnt, directCnt, reciprocalCnt = Cnts
```

```
        assert directCnt == reciprocalCnt
        assert directCnt + reciprocalCnt + unpairedCnt == len(rec_fnd)
    else:
        raise ValueError("failed reciprocity sanity check")

    return rec_num, rec_avg, rec_err, rec_fnd
```

Hence, we wrote a reciprocity sanity check loop, where *"Cnts"* is a variable that groups the values assumed by the vector rec_fnd, so it Cnts can assume at most three values: 0 for unpaired measures, 1 for direct ones and 2 for reciprocal ones. If the length of Cnts vector is equal to one, direct measures have no reciprocals, so the length of the vector *"unpairedCnts"* must be equal to the initial rec_fnd length. Instead, if the length of Cnts vector is equal to three, so involving unpaired, direct, and reciprocal measures, we split Cnts into three components and assert that the number of direct is equal to the number of reciprocal measures and that the sum of the three components is equal to the initial length of rec_fnd vector. Otherwise, the sanity checks failed. Finally, the script returns the four initial vectors concerning reciprocals information.

At this point of the processing, we also obtained the data sets of dipole-dipole configuration and its reciprocal, ready to be inverted. We must specify that since the reciprocal measures are fewer than the direct ones, the error we found in the data was extrapolated and considered valid for all data points. Thus, we inverted dipole-dipole and multi gradient data sets by using two different software, ResIPy and pygilmi. The results of the inversions will be shown in the next chapter.

At the end of the inversion results, pyBERT allows you to export the resultant Jacobian (sensitivity) matrix. The sensitivity is mathematically described by a matrix made of partial derivatives of measured resistivity as function of modelled one, but conceptually it is an expression of the coverage of a determined portion of space within the investigated domain and it can be used for the resolution analysis. Through the study of the Jacobian matrix, we can get a good representation of the sensitivity distribution and farther, including the environment and the conditions of the survey, we can trace what caused that sensitivity distribution. In our case, in both configurations, we will notice that the presence of borehole electrodes is determinant for the final sensitivity distribution.

So, we start off by extracting the Jacobian matrix and by calling it Coverage matrix A_C, made up by n columns, number of coverage model cells, and m rows, number of quadrupoles used for each configuration. We must consider that the sensitivity value of any single element is the result of the contribution of each quadrupole involved in the configuration. Under this perspective, we can estimate to what extent a single quadrupole is contributing or not to increase the coverage of a specific cell and thus we might identify some cells with a little sensitivity value.

The second step we can do is to get the covariance matrix from the initial coverage matrix by using linear algebra:

$$A_C A_C^T \div (n - 1)$$

Where A_C^T is the transpose coverage matrix and n the total number of elements. We obtain a square matrix called Covariance matrix made by the the number of quadrupoles m on both sides. This matrix is an expression of the covariance of the quadrupole combinations; hence it shows the degree of similarity of sensitivity between two quadrupoles and its variability.

As third step, still from the initial coverage matrix, we can obtain the angle matrix by following this relation:

$$arccos(A_C A_C^T \div nn^T), \quad n_i = \|a_i\|$$

So, taking the arccosine of AA^T and nn^T which respectively represent the coverage matrix and its transpose and the number of cells vector and its transpose. The double vertical bars denote the absolute value or magnitude of the vector, which is calculated as the square root of the sum of the squares of its components. This matrix shows through an angular quantity the difference between two quadrupoles in terms of sensitivity.

5) Inversions results.

In this chapter I am going to show you the results we obtained from the inversions from ERT and IP data, plus the results of the coverage, covariance, and angle matrixes we got after the Jacobian matrix analysis. Through these results I would like to estimate the depth of the water table and checking if it is coherent with the one we measured directly at the site, to assess the lithology of the site and compare it with the stratigraphic log, to verify the presence of any polarizable material as clays or buried body in the subsoil and to estimate how sensitivity distribution changes through the Jacobian matrix analysis including or not borehole electrodes in the acquisition scheme. To explain it I will show the resultant sensitivity sections for both configurations and those obtained by just three different quadrupoles.

5.1) Results of ERT data inversion.

For the resistivity sections we only show the ones from ResIPy and pygimli for both dipole-dipole and multi gradient configurations. In both cases we considered for the inversions the error threshold previously obtained from the two methods of data error assessment, decay curve analysis and reciprocal error, respectively for multi gradient and dipole-dipole configurations. Precisely, for multi gradient configuration data sets we chose 5% as error threshold, while for dipole-dipole data sets we had to increase it up to 10%. This choice kept a low number of iterations and a smooth convergence. The first consideration we can make is that the water table is well observed with the two configurations, with and without the usage of borehole electrodes. It is specified that to run an inversion without considering borehole electrodes I simply neglected those quadrupoles concerning borehole electrodes through the usage of a MATLAB script that I wrote.

Starting with the dipole-dipole resistivity section (Figure 5.1) involving borehole electrodes, we can recognize a first superficial and thin resistive layer characterized by a resistivity value of 3000 Ω.m likely due to the dry wooded soil where electrodes were placed and a dark yellow hard to not hard sand which continues for further two meters depth. The following hard flint horizon of 0,4 m thickness is not observed since the vertical resolution is not good enough due to the spacing between electrodes of 1,25 m. The initial resistive layer is interrupted by a more conductive horizon representing the brown sand in the stratigraphic log that extends from 2,40 m to 5 m depth and characterized by an average resistivity of 600

Ω.m. Still moving down in the section, we see a second resistive layer which represents the alternating of light brown and pinkish sandstone and schists which occupies a portion of subsurface ranging from 5 m to 8 m deep, showing resistivity values from 3000 Ω.m to 6000 Ω.m. This second resistive horizon enjoys a constant horizontal continuity for the whole length of the array due to the good lateral resolution that dipole-dipole configuration provides, and it partially interrupts the above conductive layer in the correspondence of the right side of the borehole. From this point on, the resistivity gradually decreases even though the lithology remains similar. In fact, despite the following strata in the stratigraphic log is represented by the alternating of dark to light brown sandstone and schists that goes from 8 m to 16 m deep, it gradually passes from a 700 Ω.m to 100 Ω.m resistivity values within a few meters. This behaviour is attributed to the water table located at 14,6 m deep and to the capillary fringe, a saturated zone above the water table where water is affected by capillary forces due to a pressure gradient. The conductive water indeed replaces the air in the pores of the geological formation making it saturated and lowering its average resistivity according to Archie's law:

$$\rho_f = \frac{a}{\phi^m S_w^n} \cdot \rho_w$$

<div align="right">(Eq. 5.1)</div>

Where a (usually near to one) is an empirical constant, m is the cementation exponent (usually near to two), n is the saturation exponent (usually near to two), ϕ is the porosity of the analyzed sample, S_w is the water saturation of the sample, ρ_w is the resistivity of the water in the sample and ρ_f is the overall resistivity of the formation. What we derive from this equation is that either by increasing the porosity or the water saturation, the total resistivity of the formation decreases. In our case, getting closer to the water table the water saturation increases making the geological formation gradually more conductive. Hence below the water table the section appears homogeneous in term of resistivity, reaching values from 70 Ω.m to 100 Ω.m, since water saturation is at its maximum and water resistivity mainly guides the formation one. The section is overlayed by the sensitivity which is represented by the white aura that assumes a "V" shape. The portion hided by the sensitivity overlay should not be considered for the final interpretation since there sensitivity assumes low values. Low sensitivity values can be translated as a poor investigation of a certain region of space and so too few data points to rely on for the inversion. In this first case, borehole electrodes are not covered since they were included in the acquisition scheme of the inversion.
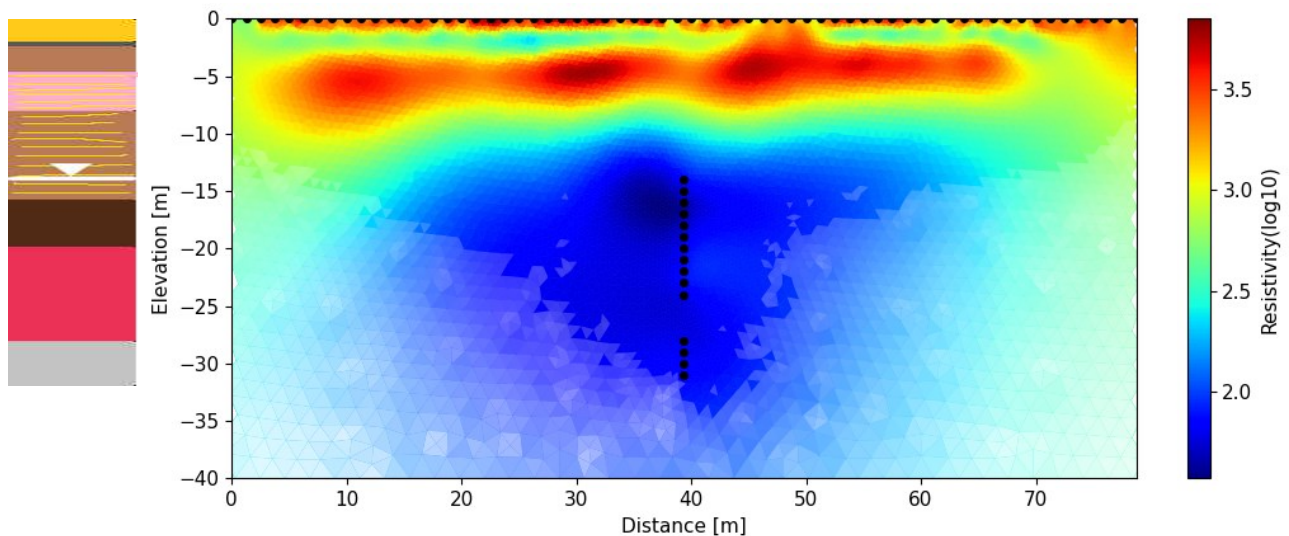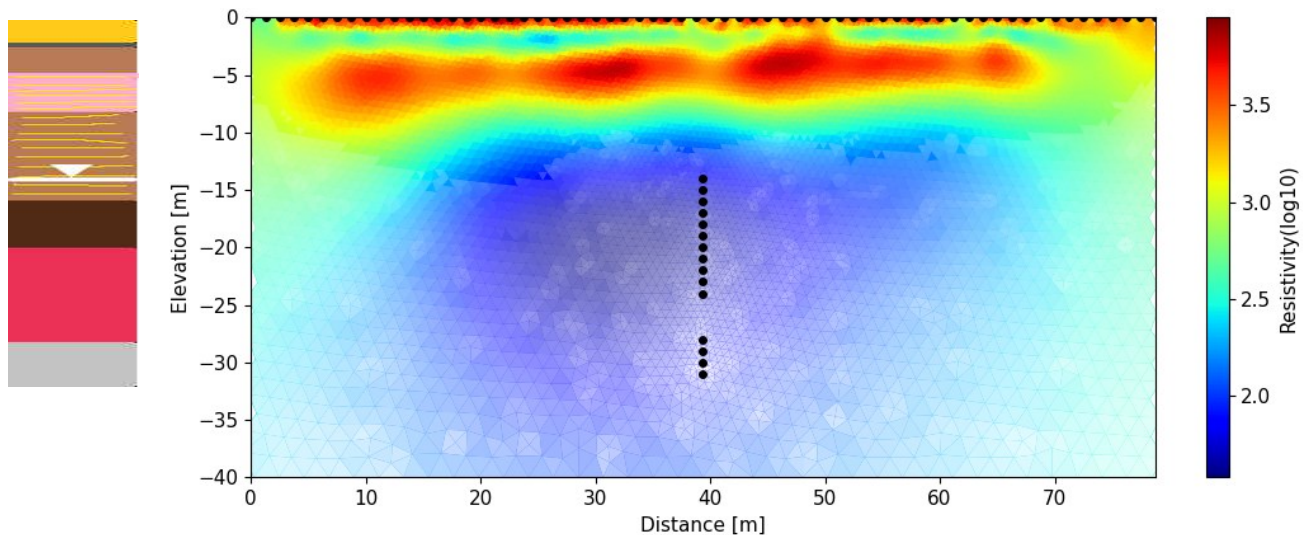
Figure 5.1 – Dipole-Dipole resistivity section involving borehole electrodes, from ResIPy. Stratigraphic log is next to the section for a better interpretation.

Moving to the dipole-dipole resistivity section without involving borehole electrodes (Figure 5.2), we can affirm that the pattern and the respective resistivity values are almost the same compared to the previous section. Indeed, until 15 m deep the main features which we can recognize are the same ones, the first shallow resistive layer due to the dry wooded soil, the following relatively conductive horizon, the second resistive layer that interrupts the above conductive one on the right side of the section and the gradual decrease in resistivity as we approach the capillary fringe and the water table. An encouraging result is that the thickness of resistive and conductive layers is equal in both the sections, with and without considering borehole electrodes. The main difference is the shape of the sensitivity overlay which covers completely the borehole electrodes. In this case it starts from about 15 m deep downward, which is reasonable since the length of the array is 80 m and the estimated penetration depth is about 16 m. It means that below that depth we have no data points we can rely on for the inversion since the deepest region of the subsoil was not investigated.

Figure 5.2 – Dipole-Dipole resistivity section without involving borehole electrodes, from ResIPy. Stratigraphic log is next to the section for a better interpretation.

Considering now multi gradient resistivity section involving borehole electrodes (Figure 5.3), it can be compared to dipole-dipole resistivity section concerning borehole electrodes in terms of resistivity and thickness of the resistive and conductive layers observed. The first main difference we notice is that the horizontal continuity of the strata is not as well respected as in dipole-dipole configuration. Indeed, the first relatively conductive layer seems not to be continuous horizontally, on the contrary it looks like that the first and second resistive layers touch each other for about half of the length of the array limiting the lateral continuity of the conductive layer. The second resistive horizon itself shows a weaker lateral continuity than the one obtained with the dipole-dipole array, especially on the left side of the section. These lateral discontinuities may be two proves demonstrating the fact that multi gradient lateral resolution is not as precise as dipole-dipole one as consequence of the different quadrupole geometries assumed. The second main difference is that on average multi gradient configuration shows slightly lower resistivity values compared to dipole-dipole. The third difference regards the shape of the sensitivity overlay. In this case, the "V" shape is still present, but it starts at a depth between 20 m and 25 m deep, while for dipole-dipole configuration it starts at 15 m deep. This aspect of the interpretation further characterizes the difference between dipole-dipole and multi gradient configuration, making this latest more reliable as we move toward the lateral limit of the domain.
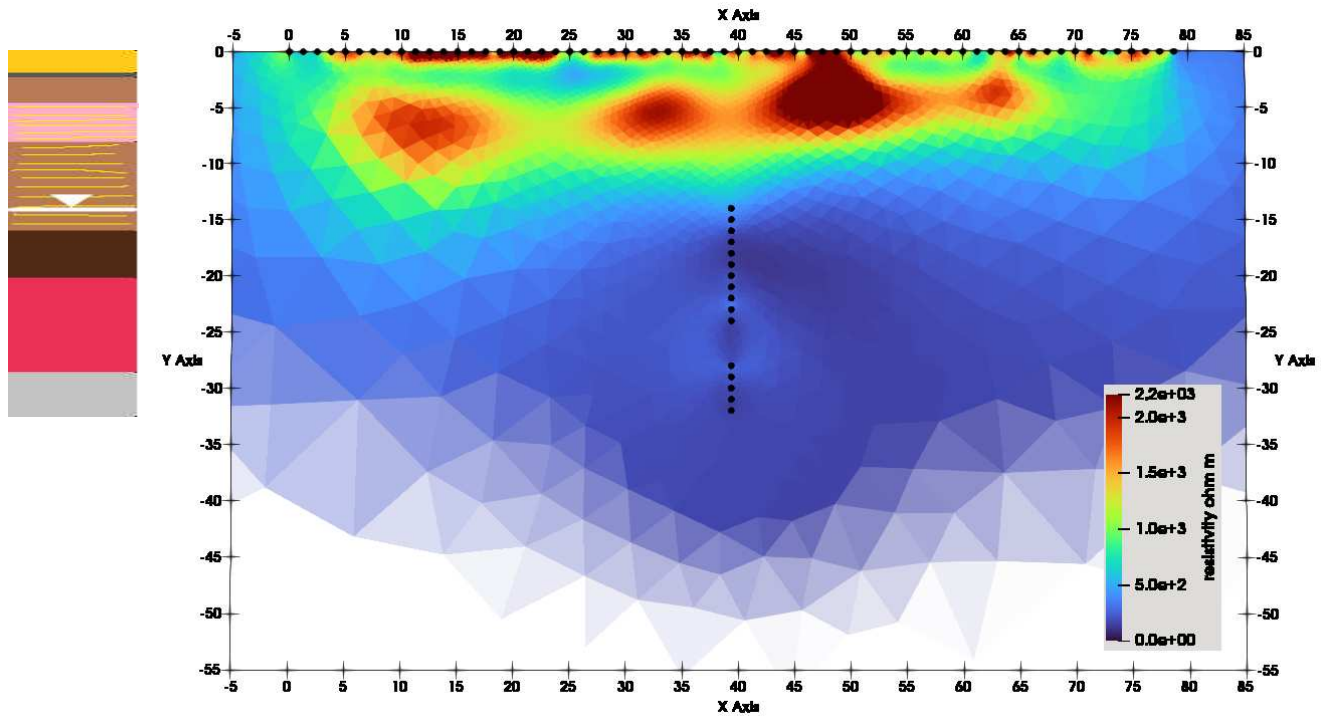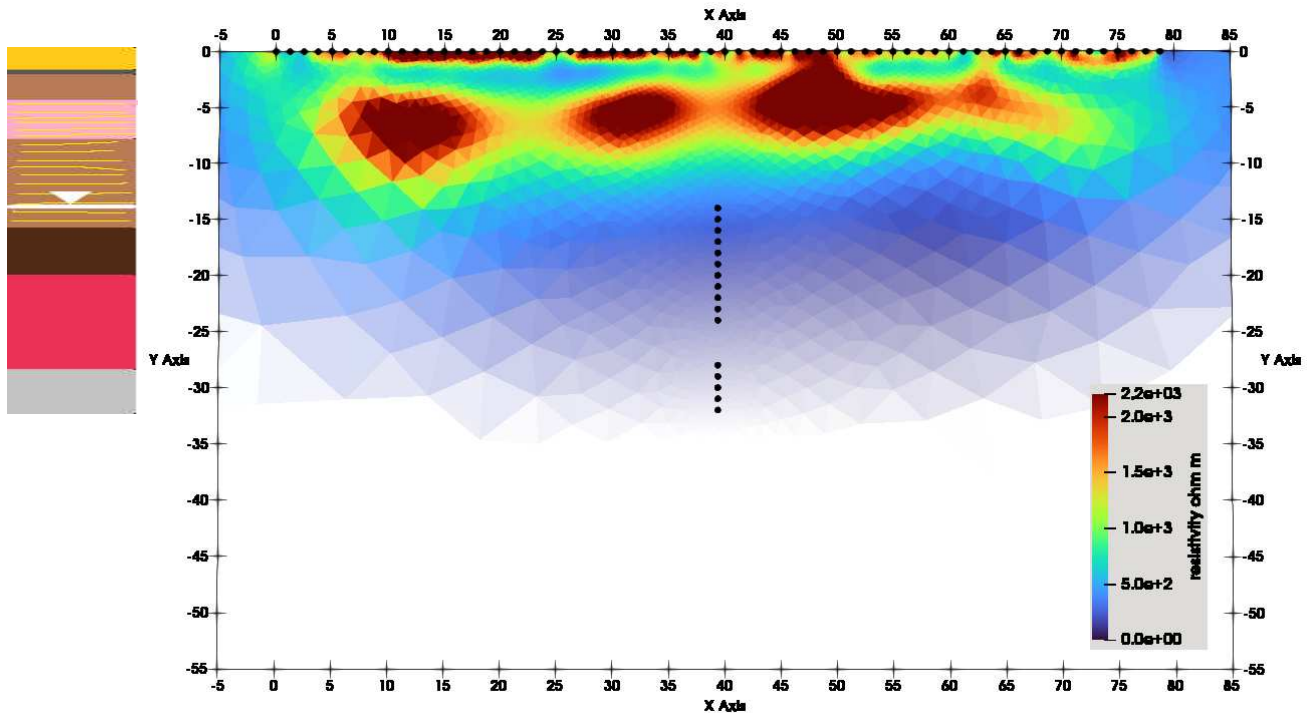
Figure 5.3 – Multi gradient resistivity section involving borehole electrodes, from pygimli. Stratigraphic log is next to the section for a better interpretation.

Lastly, moving to the multi gradient resistivity section without involving borehole electrodes (Figure 5.4), main resistive and conductive layers and their lateral discontinuities are still shown, so the coherence with the stratigraphic log is still respected. Nevertheless, without considering borehole electrodes the lateral continuity of both, first conductive and second resistive layers look more defined compared to the previous inversion concerning borehole electrodes. As in dipole-dipole case, the thickness of the layers along both multi gradient resistivity sections looks coherent. One more common point that links multi gradient and dipole-dipole configurations without borehole electrodes is the shape of the sensitivity overlay. Indeed, it is represented by the whitish horizon starting from 16 m – 17 m deep, which is reasonable since the penetration depth is still estimated to be about 16 m.

Figure 5.4 – Multi gradient resistivity section without involving borehole electrodes, from pygimli. Stratigraphic log is next to the section for a better interpretation.

5.2) Results of complex resistivity inversion.

For the complex resistivity σ^* and chargeability inversions we used only ResIPy, and we increased the error threshold, 7% for multi gradient and 15% for dipole-dipole configurations. Complex resistivity inversion is represented by a section of the following quantities, real conductivity component σ', imaginary conductivity component σ'' and phase angle. We also obtain a chargeability section. Nevertheless, we must specify that real and imaginary components of conductivity and phase angle were carried out from multi gradient configuration without borehole electrodes since they are cause for artifacts in the final inversion as well as dipole-dipole configuration dataset probably due to a not good enough signal to noise ratio, so the interpretation stops at a depth of about 16 m. While chargeability section was carried out with pygimli from multi-gradient dataset involving borehole electrodes.

Starting from real conductivity component σ' (Figure 5.5), it is expressed in (S/m) in log scale. It precisely recognizes and follows the main layers we already described in the resistivity sections, starting with the shallowest less conductive medium involving dry wooded soil where electrodes were placed and a dark yellow hard to not hard sand which continues for two meters depth. Moving down we

67

meet a more conductive horizon representing the brown sand in the stratigraphic log and then we have a second less conductive layer representing the alternation of light brown to pinkish sandstone and schists. We are still able to observe the discontinuity in the conductive layer due to the contact between the first and the second resistive layers on the right side of the borehole. Then real conductivity gradually increases due to the presence of the water table at 14,6 m deep and in the above vadose zone. It is coherent for the real conductivity component σ' section to show the same distribution as the resistivity section since these two parameters express the same property of the subsurface, to resist the flow of current, and they are not involved in any polarisation phenomena. Indeed, the measured electric field related to the real component of conductivity is in phase with the injected one.
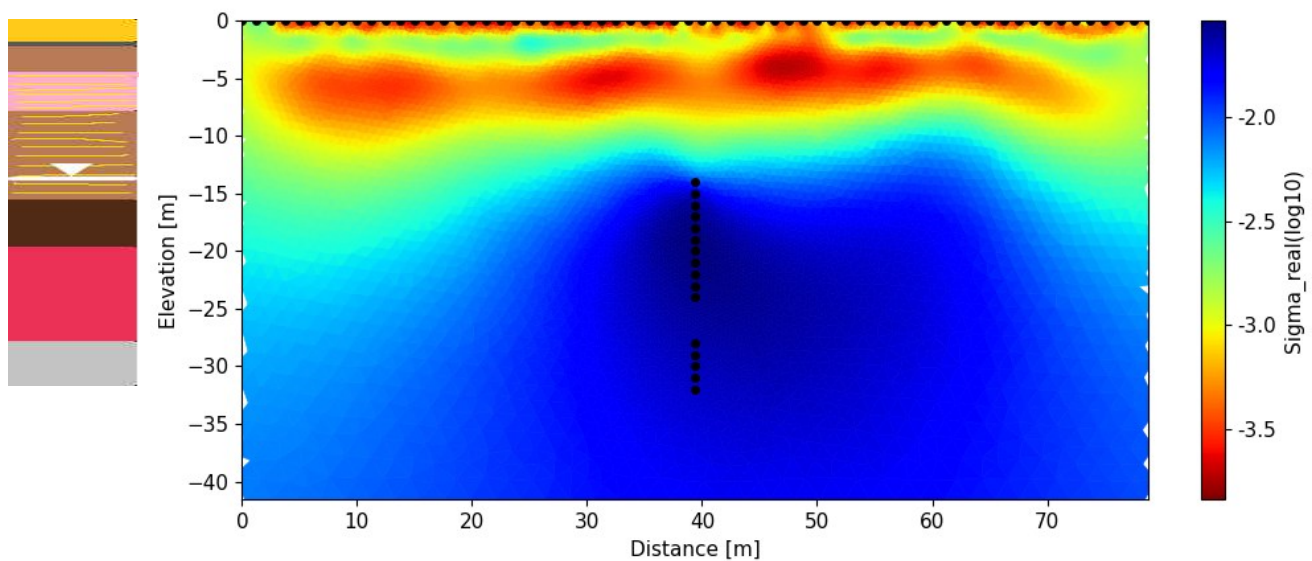
Figure 5.5 – Real conductivity component section, σ'. Stratigraphic log is next to the section for a better interpretation.

About the imaginary conductivity component σ'' (Figure 5.6), it is expressed in (S/m) in log scale as well and it shows values three orders of magnitude smaller than σ'. The alternation of less and more conductive layers is still observed as well as the main horizontal discontinuity in the conductive layer. Further, since the relative depth at which the water table is located, we can assume that the shallow portion of the section involving the three alternation of resistive and conductive layers is dry. This means that the sharp contrasts shown in σ' and σ'' sections are mainly guided by lithology, so by mineralogy and granulometric distribution of the geological formation. The sharp contrasts hence represent a contrast in grain size distribution and mineralogy of the units, superficially described by the stratigraphic log that shows an alternation of sand (first three units) and sandstone. The

explanation for the imaginary conductivity component σ '' section to be like the real component one σ ' is lithological. Indeed, finer grain sizes lower the resistivity and increase the polarisation and vice versa. Furthermore, finer grain sizes can be understood both ways of actual finer grain sands, either sand including a higher clay fraction.
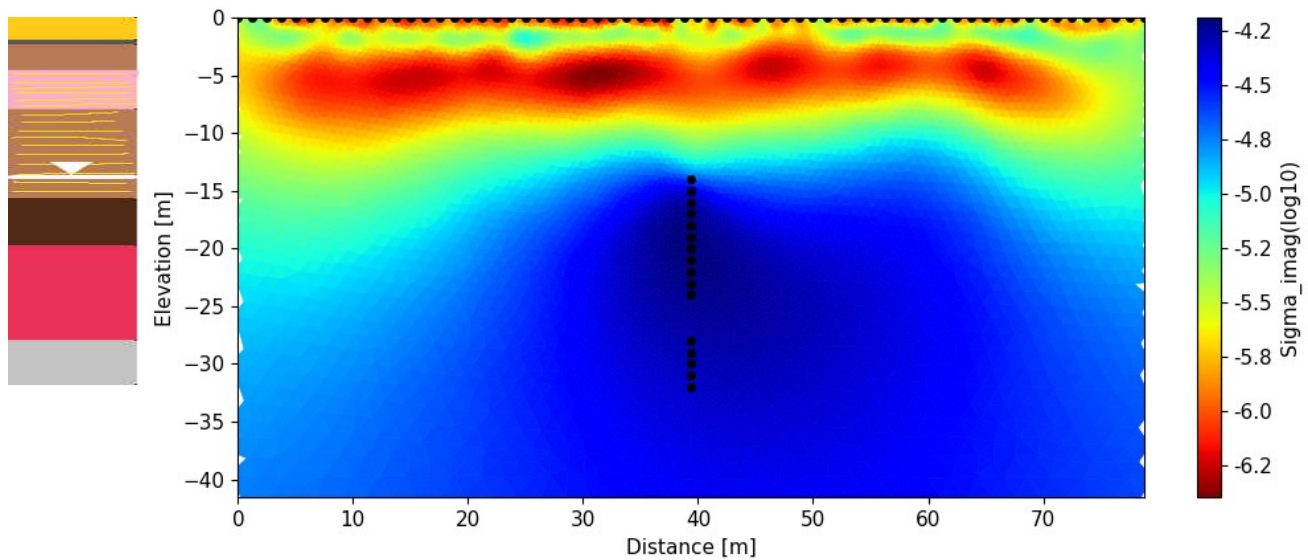

Figure 5.6 – Imaginary conductivity component section, σ''. Stratigraphic log is next to the section for a better interpretation.

To conclude, comparing phase angle section (Figure 5.8) in $mrad$ and chargeability section (Figure 5.7) in mV/V, they show the same main characteristics. The shallow portion of both sections is the only one with a relative high value of polarization, especially on the right side of the borehole, due to the presence of organic matter on the uppermost part of the soil. While the rest of the sections do not show any polarization by assuming a smooth behaviour of relatively small values of $mrad$ and mV/V. This smooth behaviour can be attributed to a lack of clay minerals in the alternation of geological units. Chargeability and phase angle sections look similar since they are two different representations of the same polarisation phenomenon. Furthermore, it is reasonable for the phase angle section to look mostly smooth since the imaginary and real conductivity components sections look very similar due to a lack of polarisation effect and whereas phase angle is ruled by equation 3.77 described in chapter 3.
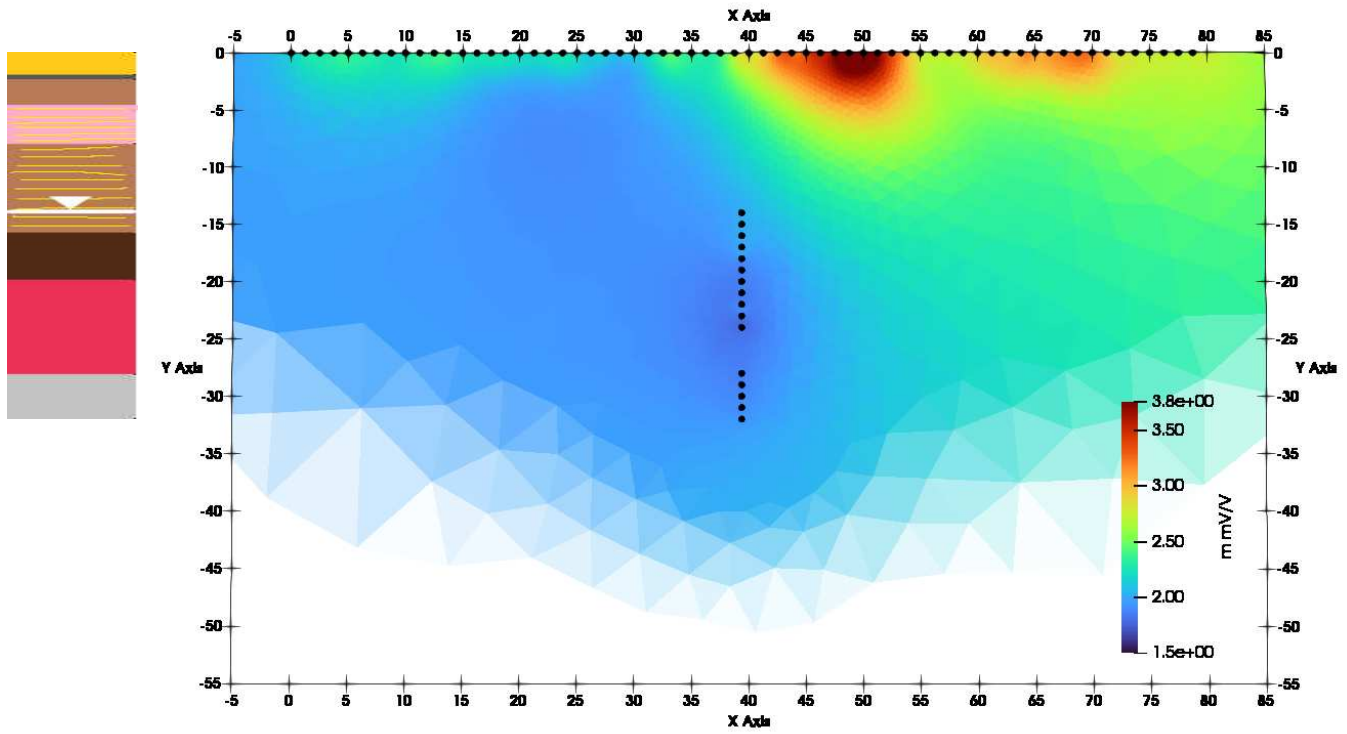
Figure 5.7 – Chargeability section obtained with pygimli. Stratigraphic log is next to the section for a better interpretation.
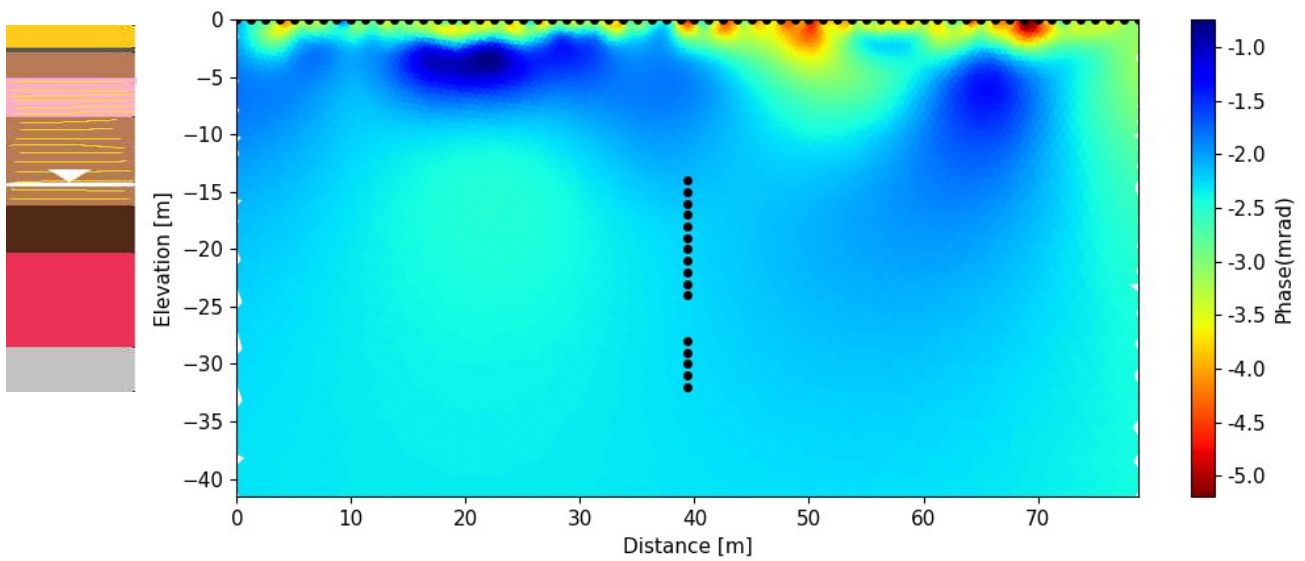

Figure 5.8 – Phase angle section obtained with ResIPy. Stratigraphic log is next to the section for a better interpretation.

5.3) Coverage, covariance, and angle matrices.

Then we performed an analysis on how the sensitivity distribution changes with and without considering borehole electrodes for both configurations, multi gradient and dipole-dipole. To do so we focused our study on the sensitivity matrix (Jacobian matrix) obtained directly from the inversion. The following proceedings were possible thank to a python script kindly provided by Doct. Luca Peruzzo.

Starting from the coverage matrix (Figure 5.10 and 5.9), expressed in log scale, it is the resulting Jacobian matrix we obtain at the end of the last iteration of the inversion process. The columns represent the cells (elements) of the model, while rows are the measurement quadrupoles. A horizontal line is then the expression of a single sensitivity section created by that single specific quadrupole. Vertical red lines show that many quadrupoles cover that specific cell, while vertical blue lines show a cell with lack of coverage. Horizontal red lines show that the quadrupole does provide a good coverage to a specific range of cells, while mainly blue horizontal lines show those quadrupoles focus their coverage on small portions of the domain. Surely, the distribution of both vertical and horizontal red and blue lines depends on the configuration we are considering, so we will expect some differences between dipole-dipole and multi gradient configurations. Comparing Jacobian matrix from dipole-dipole and multi gradient data sets inversions, we can notice that multi gradient configuration involves more quadrupoles than dipole-dipole one and that both show two main red vertical lines in correspondence of the 2000th cell and about the 3300th cell. Given the thickness of these vertical lines, the cells with a high value of coverage are more than one. The reason why two different configurations show a high value of coverage in correspondence of the same elements of the model may be attributed to the fact that for both configurations that region of domain was well investigated perhaps due to its central and not yet deep position and for proximity to the electrodes. Overall, dipole-dipole configuration shows high coverage values, so a high red vertical lines distribution, between the 1500th and 3300th cell. Horizontal blue lines, each including more than a quadrupole, are instead clearly visible between the 1st and 500th quadrupole and one is located at about the 1000th quadrupole. Vertical blue lines are present mostly from about the 4100th element on. Still in these cases, if we zoomed the image, we would notice that the quadrupoles and elements involved in the coverage are more than one. Multi gradient configuration shows a high concentration of vertical and horizontal red lines between the 1500th and 4500th element of the model. About horizontal blue lines, they are mainly present starting from the 1000th quadrupole till the bottom and the two top edges of the figure, as well as vertical blue lines.
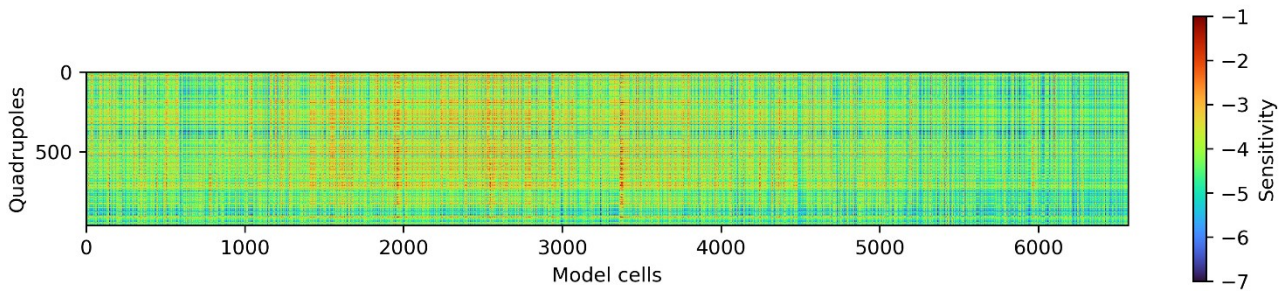
Figure 5.9 – Coverage matrix representation obtained from dipole-dipole configuration.
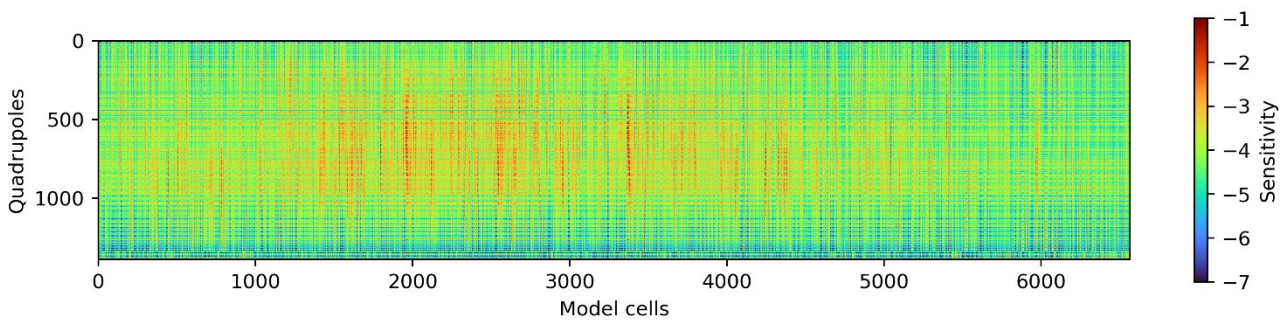

Figure 5.10 – Coverage matrix representation obtained from multi gradient configuration.

About covariance matrixes (Figure 5.11), on both axes the quadrupoles are represented. We decided to arrange the quadrupoles along both axis such that from the origin to their end the number of the borehole electrodes involved in the quadrupoles gradually increases, such that we should be able to compare the degree of similarity between quadrupoles involving borehole electrodes and quadrupoles not involving borehole electrodes. Covariance matrixes is shown by red and blue colours which, respectively, represent high similarity degree and low similarity degree between quadrupoles. In the case of dipole-dipole covariance matrix, the highest similarity degree between electrodes is found in the main red areas having the shape of two squares, on the top left side of the image until the 600th quadrupole in both axes, and on the bottom right side, from the 600th quadrupole on in both axes. It is reasonable to think so, since these two portions of the image refer to quadrupoles having a similar number of borehole electrodes. The lowest similarity degree instead is registered in the remaining two rectangular portions of the image, the first one from the 600th quadrupole on for y axis until the 600th quadrupole for x axis, and the second one until the 600th quadrupole for y axis and from the 600th quadrupole on for y axis. Doing so, we identified the quadrupoles that differ the most in term of sensitivity compared to each other. More precisely, as we expected, we proved visually (but still qualitatively) that the biggest difference in term of sensitivity is given between quadrupoles involving

72

borehole electrodes and quadrupoles not involving borehole electrodes. About the multi gradient covariance matrix, the patterns of high and low similarity degree between quadrupoles are like dipole-dipole one. Indeed, we can recognize two regions of high sensitivity similarity degree on the top left and on the bottom right corners, while two regions of low sensitivity similarity degree on the top right and on the bottom left corners. Still, big sensitivity differences are associated to a comparison between quadrupoles involving and not borehole electrodes.
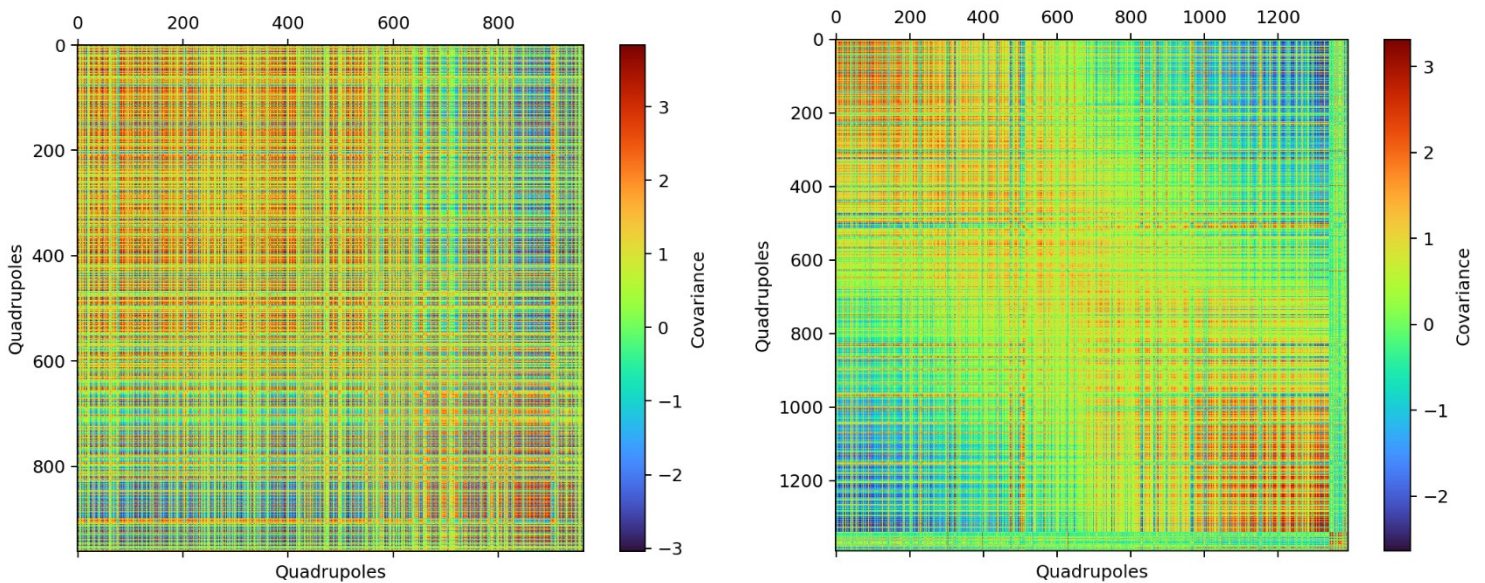
Figure 5.11 – Comparison between covariance matrices obtained from dipole-dipole (left image) and multi gradient (right image) configurations.

Lastly, angle matrix (Figure 5.12) gives a more quantitative estimation (rad) of the sensitivity similarity degree between quadrupoles and their arrangement along the axis is the same of covariance matrix. What emerges for dipole-dipole angle matrix is a similar pattern, comparable to low sensitivity similarity degree rectangular regions in covariance matrix, showing the highest angular values (red rectangular zones), which is coherent to what we said so far. Indeed, with such quantification, we can notice that the quadrupoles having the biggest difference in sensitivity are the ones involving and not the borehole electrodes, according to covariance matrix. About multi gradient configuration angle matrix, the concept is the same. Regions showing highest angular values are superimposable to those ones showing lowest covariance values. In both angle matrixes it is interesting to notice that the top left bottom right diagonal is made of angular values equal to zero since it is comparing the same quadrupoles throughout its length.
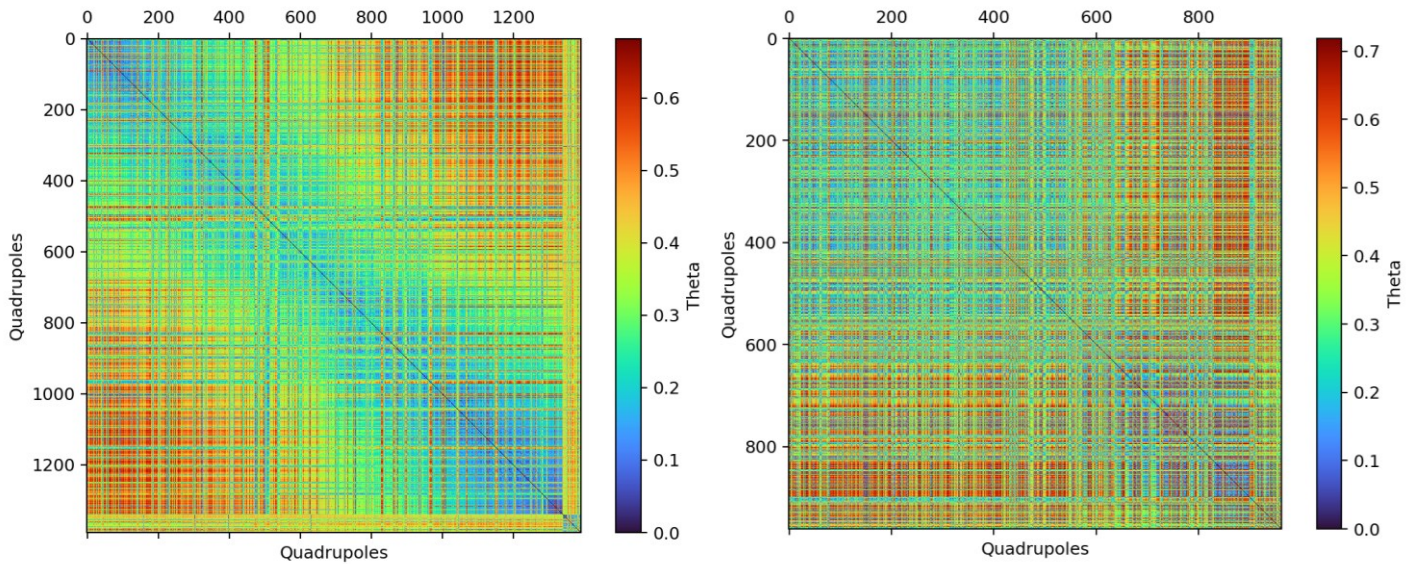
Figure 5.12 – Comparison between angle matrices obtained from dipole-dipole (right image) and multi gradient (left image) configuration.

As last point, I am going to compare the sensitivity sections obtained as sum of each quadrupole contribution for multi gradient and Dipole-Dipole configurations. Indeed, the sensitivity value in each element of the discretized domain is equal to the sum of the sensitivity quantity brought by each quadrupole. Those elements of the domain showing relative higher values of sensitivity enjoy a good coverage, since the sum of the quadrupoles sensitivity contribution results high. It can be translated as a good reliability for the final inversion. Sensitivity may show both positive and negative values since it is mathematically described as a derivative, hence if the gradient is negative, the final sensitivity results negative and vice versa for a positive gradient.

The sensitivity section for multi gradient configuration (Figure 5.13) from resultant Jacobian matrix shows in the shallow portion a specular pattern of high coverage on the left and right side of the borehole, while it doesn't seem to be there a great sensitivity continuity between the shallower and borehole portions of the section. Instead, looking at the sensitivity section for Dipole-Dipole configuration (Figure 5.14) we can notice a little inequality in terms of its distribution. Indeed, sensitivity to the left of the borehole reaches a deeper portion in the section than to the right side. But, on the other hand, shallower and borehole sensitivity chunks seem to be well connected each other showing good continuity. These two main distinctions between multi gradient and Dipole-Dipole configurations sensitivity sections are due to the different specific geometry of the quadrupoles. Furthermore, the distinction in sensitivity distribution between the two configurations can be

observed by looking at the covariance and angle matrices whereas they show different patterns.
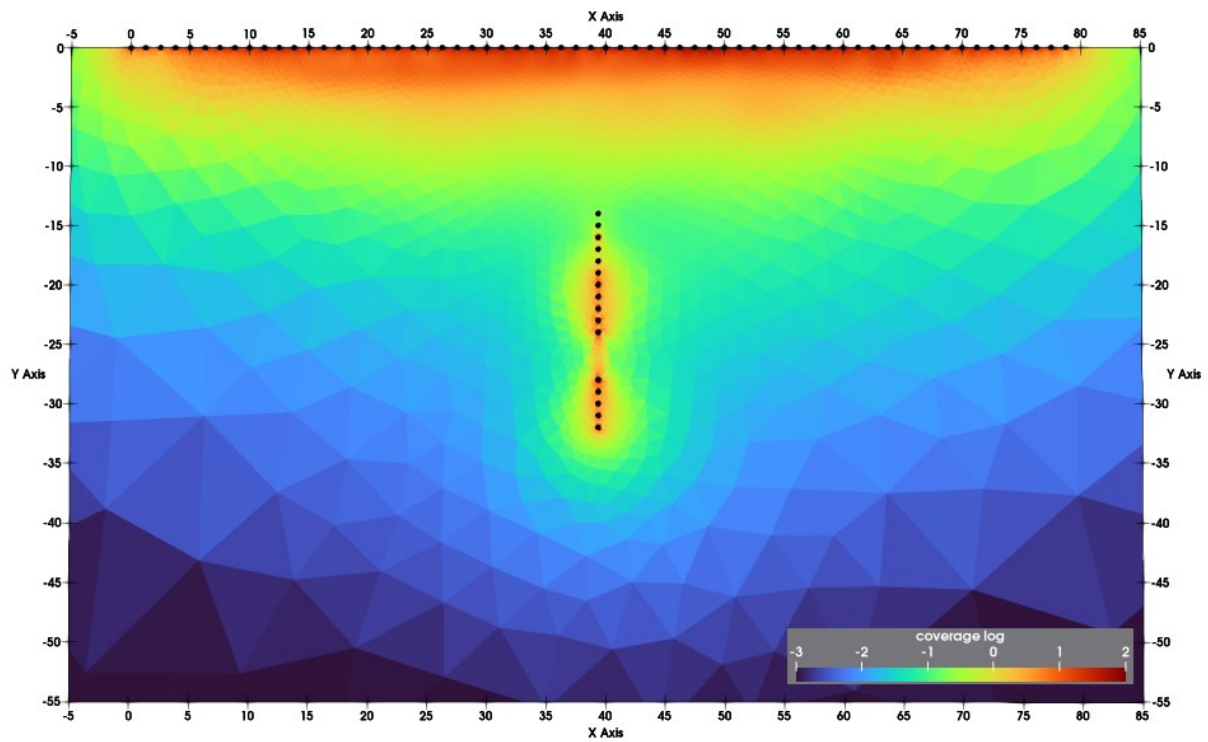

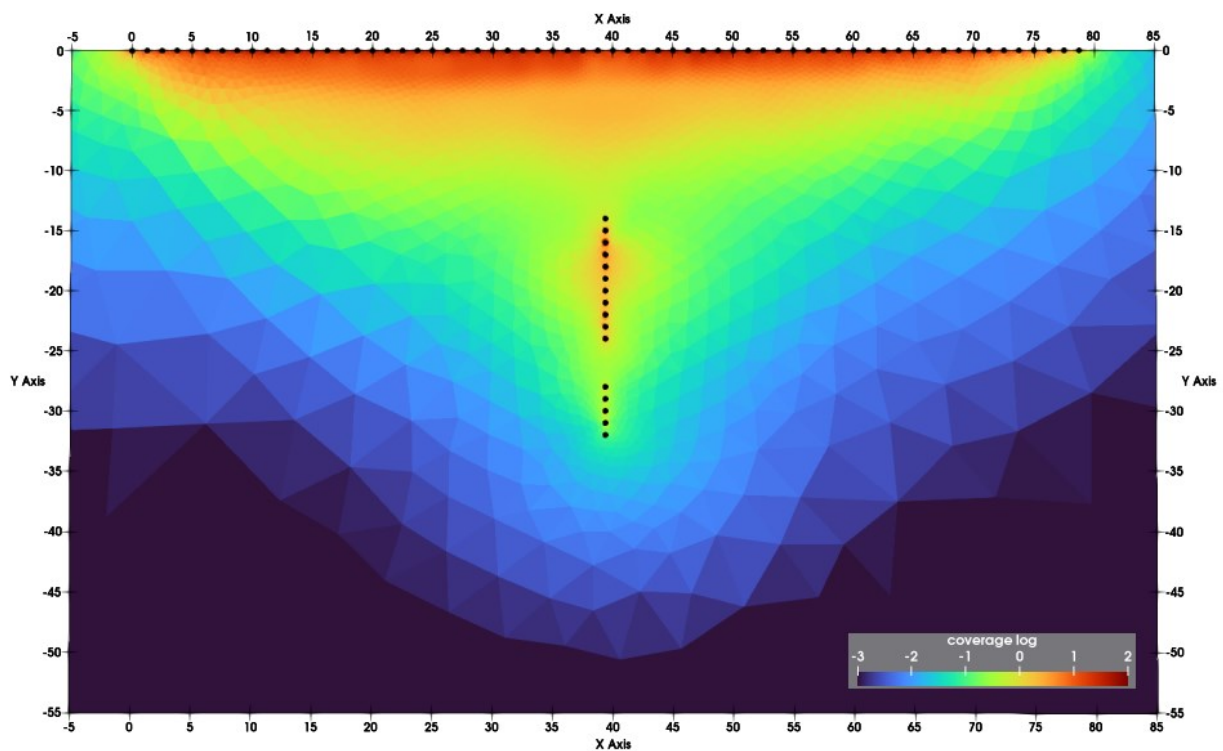Figure 5.13 – Sensitivity section obtained from multi-gradient configuration.

Figure 5.14 – Sensitivity section obtained from dipole-dipole configuration.

To better understand how sensitivity section is created, let's analyse the following three figures showing the sensitivity sections produced by three single quadrupoles involving and not borehole electrodes. These sections were included in the overall sum of all quadrupole's contribution to the final sensitivity section for multi gradient configuration and, as a matter of fact, their scale is much lower than the final sensitivity section. The first two quadrupoles (Figure 5.15 and 5.16) involve just land electrodes and as we can see the highest sensitivity values are included in the most superficial portion of the figure, while the third quadrupole (Figure 5.17) includes three land electrodes and a borehole one, thereby causing the sensitivity to reach deeper portions in the section. First and second quadrupoles result to be quite similar in terms of sensitivity patterns, while the difference between the first (or second) and the third one becomes marked. Hence, by analysing the similarity degree of those quadrupoles from a sensitivity point of view through Covariance matrix, in the first case we would notice an element of the matrix with low covariance value and another element with a bigger one in the second case.
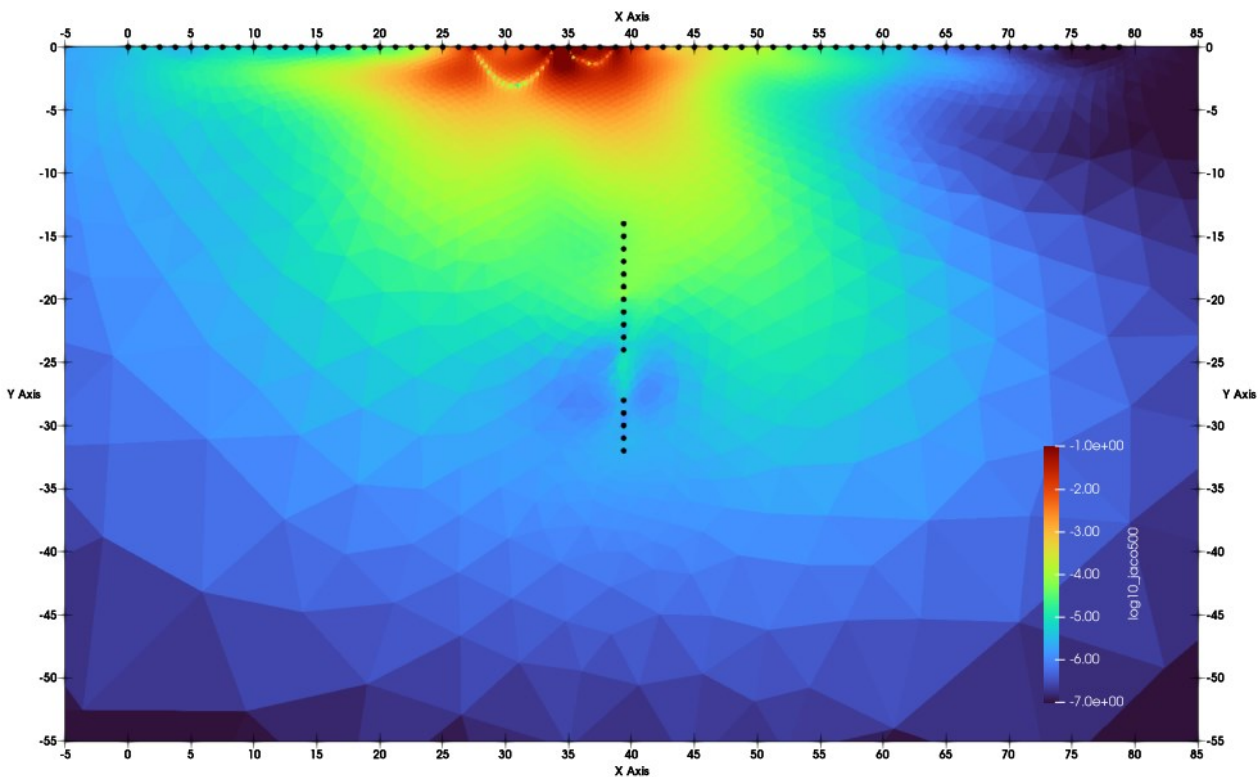

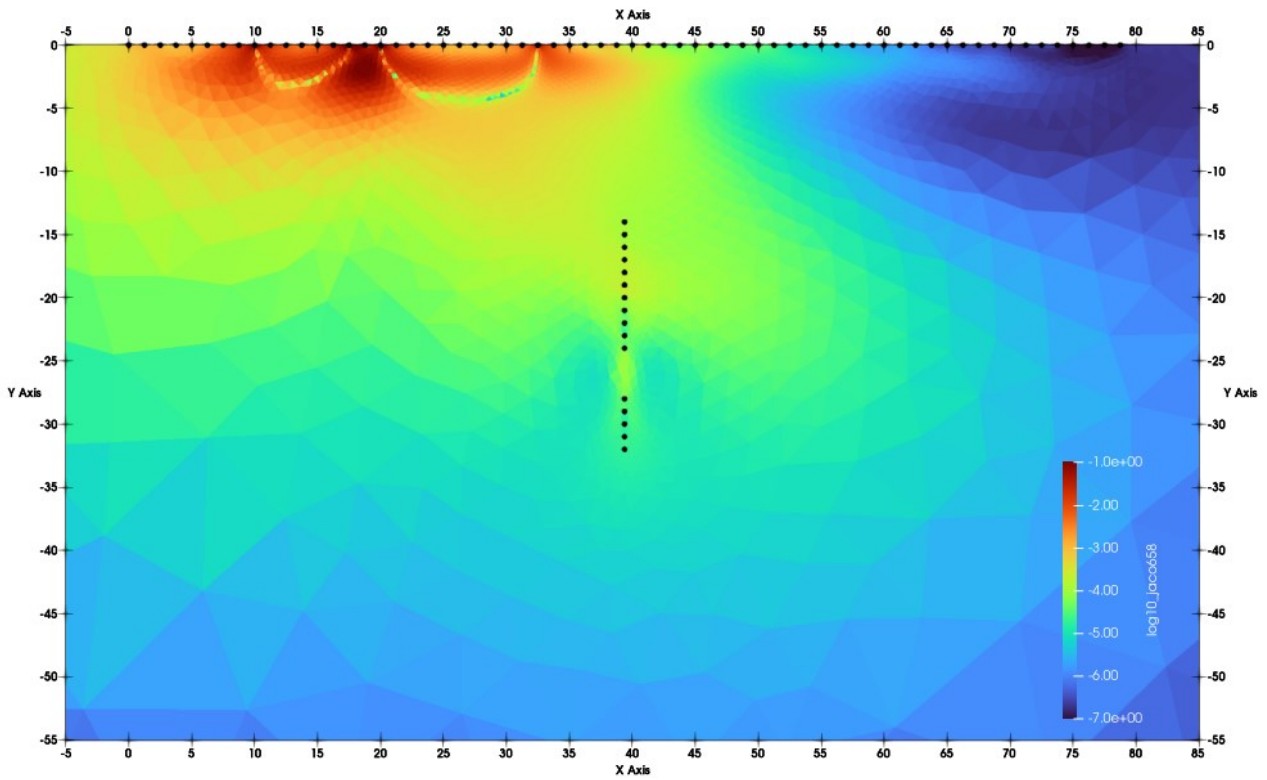Figure 5.15 – Sensitivity section obtained from a single quadrupole involving land electrodes.

Figure 5.16 – Sensitivity section obtained from a single quadrupole involving land electrodes.
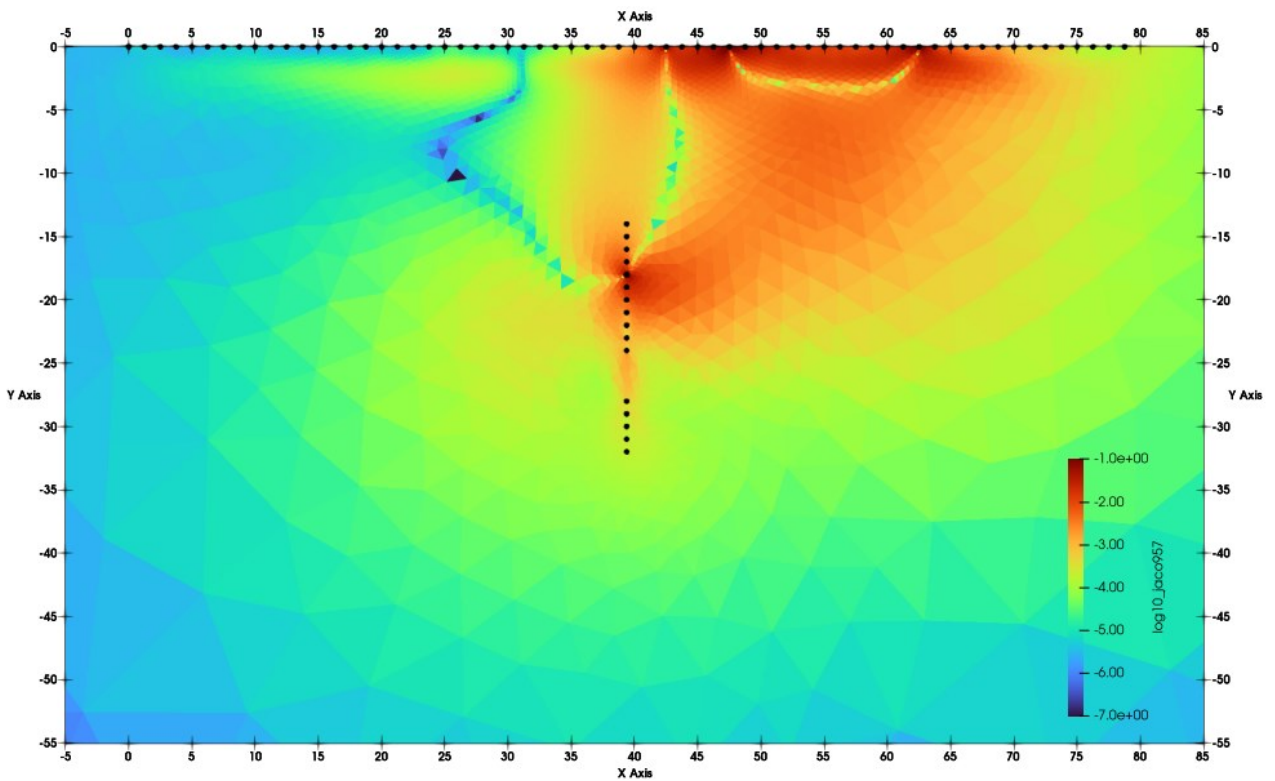

Figure 5.17 – Sensitivity section obtained from a single quadrupole involving three land electrodes and a borehole one.

To conclude, since we explained how a sensitivity section is made, we can compare and explain why in this case of study sensitivity sections do differ considering and not borehole electrodes in both configurations. What we can clearly notice is that sensitivity sections carried out without including borehole electrodes in the acquisition array (Figure 5.18 and Figure 5.19) show in both cases a high coverage degree only in the first 10m, the shallowest portion of the domain. This is explained why all the quadrupoles involve only on land electrodes, and so every single sensitivity section obtained by single quadrupoles do not involve the deep portion of the domain. Therefore, their final sum must produce a final sensitivity section that shows a good coverage value in its shallowest portion. In this regard, the application and the study of the covariance and angle matrices is another way to look at the same phenomenon. Indeed, both matrices representation show, in a qualitative and a more quantitative way respectively, how sensitivity distribution changes across the domain by increasing the number of borehole electrodes in the quadrupoles.
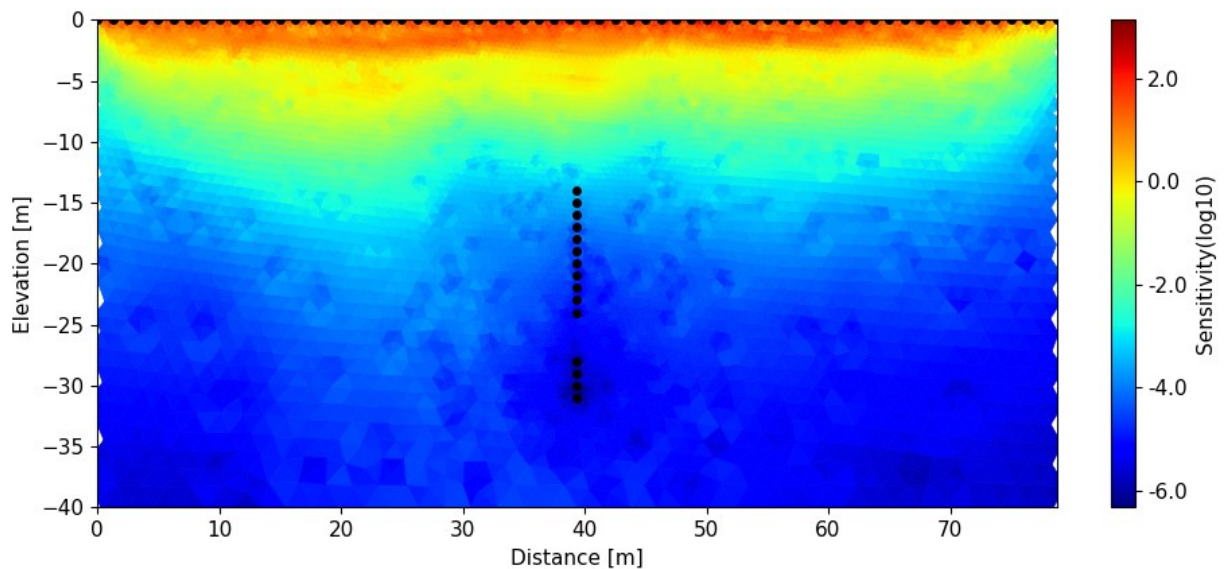

Figure 5.18 – Sensitivity section obtained from Dipole-Dipole configuration without involving borehole electrodes, ResIPy.
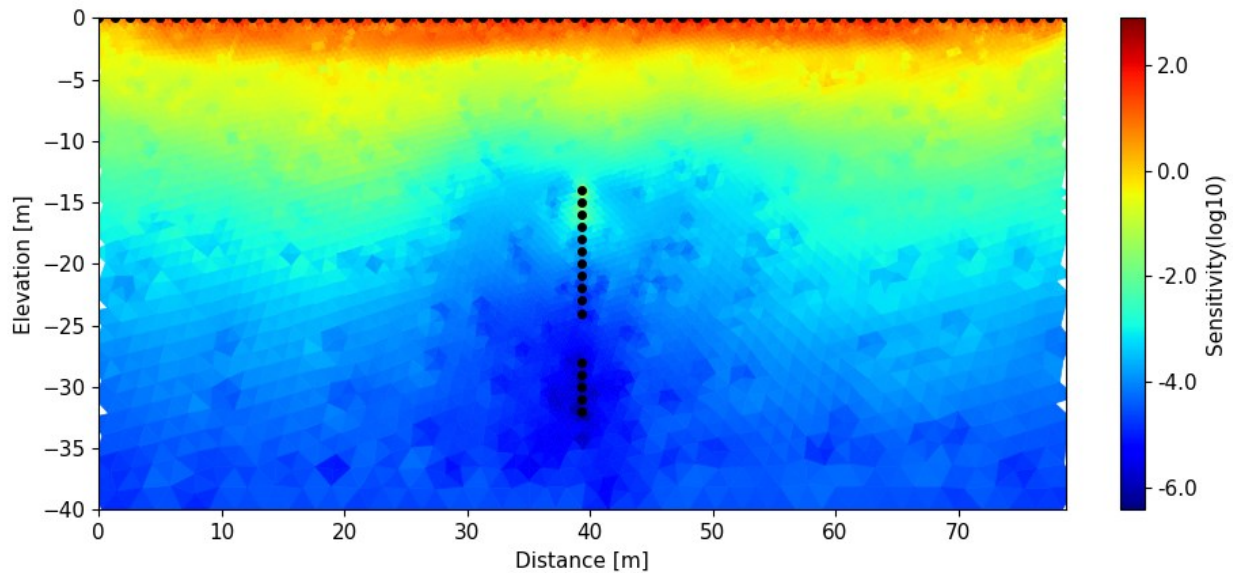
Figure 5.19 – Sensitivity section obtained from multi-gradient configuration without involving borehole electrodes, ResIPy.

6) Conclusions.

From the resistivity analysis we carried out, we can recognize a shallower alternation of resistive and conductive layers which can be coherently traced back to the geological units present in the stratigraphic log up to the beginning of the water table. Speaking of the water table itself, we can claim to be able to see it with the resistivity section in both cases, involving and not the borehole electrodes in the data sets for the two configurations, dipole-dipole and multi gradient, at the same depth of the measure we performed in situ. Hence, the chosen configurations with increasing skip, despite we neglected borehole electrodes, provided enough signal to noise ratio at sufficient depth to detect the water table.

Real and imaginary components of complex conductivity faithfully trace resistivity sections, further distinguishing the presence of different geological units for physical and mineralogical properties. At the same time, they look similar for lithological/petrophysical reason since the lack of polarisable materials does not produce any significant polarisation effect. It would be interesting to perform some specific geotechnical studies on the log samples to define the distribution of some physical and chemical properties as granulometry, porosity and mineralogy to better

interpret and to assign a clearer physical meaning to the real and imaginary components of complex conductivity.

Phase angle and chargeability sections equally further confirm the absence of clays in the section by keeping a smooth and low value of chargeability (mV/V) and phase angle $(mrad)$, except for the surface horizon which shows relative high phase and chargeability values due to the electrode's polarisation itself and the organic soil. Further, we can affirm that the investigated domain is characterized by the absence of buried polarisable objects and contaminants, despite it was not the purpose of the investigation.

The study of the Jacobian (sensitivity) matrix through the usage of statistical and linear algebra tools which translate in coverage matrix, covariance matrix and angle matrix, provided us with a qualitative and a more quantitative readings about the difference in sensitivity distribution obtained with and without considering boreholes electrodes in the data sets. As expected, from this study we can state that borehole electrodes guide the sensitivity distribution by increasing the coverage in the deepest portion of the domain, also remarked by comparing the sensitivity sections. Nevertheless, we can notice some heterogeneities. Indeed, borehole electrodes are not the only factor that rules the sensitivity distribution: electrodes spacing, and superficial electrodes positioning are two examples.

Overall, we can conclude that electrical resistivity tomography and time domain induced polarisation geophysical methods provided complementary results that can be matched for an accurate hydrogeological characterisation of the investigated site. Furthermore, covariance and angle matrices turned out to be two reliable techniques for the study of the sensitivity distribution as function of the acquisition array geometry.

7) **Bibliography.**

1. Ruthy I., Dassargues A. (2015). Carte hydrogéologique de Wallonie, Planchettes Chastre - Gembloux n° 40/5-6. Ed. Service public de Wallonie, Direction des Eaux Souterraines (SPW ARNE), Belgique. Dépôt légal D/2015/12.796/2. ISBN 978-2-8056-0173-6.

2. University of Liège. (2015). *Raport final sur les essais de captage menés au Sart-Tilman* (R-2015-026). AQUALE Ecofox Développement.

3. La Brecque, D., Daily, W. A., & Adkins, P. (2007). Systematic errors in resistivity measurement systems. *Symposium on the Application of Geophysics to Engineering and Environmental Problems 2007*. https://doi.org/10.4133/1.2924620

4. Binley, A., & Kemna, A. (2005a). DC Resistivity and Induced Polarization Methods. *Springer EBooks*, 129–156. https://doi.org/10.1007/1-4020-3102-5_5.

5. Kemna, A. K. (1999). *Tomographic Inversion of Complex Resistivity: Theory and Application* [PhD dissertation]. Bochum University.

6. Kemna, A., Räkers, E., & Binley, A. (1997). Application of complex resistivity tomography to field data from a kerosene-contaminated site. *3rd EEGS Meeting*. https://doi.org/10.3997/2214-4609.201407300

7. Mwakanyamale, K., Slater, L., Binley, A., & Ntarlagiannis, D. (2012). Lithologic imaging using complex conductivity: Lessons learned from the Hanford 300 Area. *Geophysics*, *77*(6), E397–E409. https://doi.org/10.1190/geo2011-0407.1

8. Flores-Orozco, A., Gallistl, J., Bücker, M., & Williams, K. H. (2018). Decay curve analysis for data error quantification in time-domain induced polarization imaging. *Geophysics*, *83*(2), E75–E86. https://doi.org/10.1190/geo2016-0714.1

Ringraziamenti

In ordine sparso. Ringrazio i miei genitori e mia sorella per il supporto emotivo donatomi durante alcuni dei momenti più difficili della mia vita, sebbene sia solo agli inizi. Ringrazio i miei amici per i momenti di spensieratezza che abbiamo condiviso, rimedio formidabile contro le avversità del destino. Spendo due parole in più su Arianna, fedele compagna di avventure in terre germaniche, per i bei momenti vissuti e le confidenze scambiate in quel di Bonn. Ringrazio il Prof. Antonio Galgaro per la sua pazienza e costanza nel seguirmi a distanza, il Prof. Jacopo Boaga per l'aiuto e la disponibilità con la quale mi ha accettato come tesista ed il Dott. Luca Peruzzo per la sua professionalità, senza la quale non sarei qui oggi. Un'umile lode anche a te Alberto, ce l'hai fatta.

Acknowledgment

In no order. I thank my parents and sister for the emotional support they gave me during some of the most difficult moments of my life, even though it is only just beginning. I thank my friends for the moments of light-heartedness that we shared, a formidable remedy against the adversities of fate. I'll spend a few more words on Arianna, faithful companion on adventures in Germanic lands, for the beautiful moments experienced and the confidences exchanged in Bonn. I thank Prof. Antonio Galgaro for his patience and perseverance in following me remotely, Prof. Jacopo Boaga for the help and availability with which he accepted me as a thesis student and Dr. Luca Peruzzo for his professionalism, without which I wouldn't be here today. Humble praise to you too Alberto, you did it.